Contract No. DTFACT-15-D-00007

TASK ORDER 015 – REFLECTIVE CRACKING SUPPORT

DELIVERABLE 4.10.2.1 REFLECTIVE CRACKING INDOOR PHASE VI COMPREHENSIVE REPORT

November 2019

Prepared by Gemini Technologies, Inc.
For SRA International, Inc., a subsidiary of
General Dynamics Information Technology

GENERAL DYNAMICS
Information Technology

TABLE OF CONTENTS

EXECUTIVE SUMMARY VI

1. INTRODUCTION 1

1.1 Objectives 1
1.2 Test Overlay And Instrumentation 1

2. OVERLAY CONSTRUCTION 2

3. SHAKE-DOWN TEST 9

4. FORMAL TEST 11

4.1 Temperature Control 12
4.2 Performance Monitoring 13
4.3 Observations 15

5. OVERLAY DETERIORATION 19

6. DAMAGE ANALYSIS 20

6.1 Failure Strain 21
6.2 Strain Energy 25
6.3 Fracture Energy 26

7. CRACK PROPAGATION ANALYSIS 28

8. EFFECT OF EXTREME COOLING CYCLE 31

8.1 Strain Response 31
8.2 Strain Energy 33
8.3 Fracture Energy 34

9. IMPLEMENTATION OF RCIP-VI TEST DATA 35

9.1 Step 1: Crack Initiation 35
9.2 Step 2: Crack Propagation 36
9.3 Step 3: Finite Element Model Validation 36

10. CONCLUSIONS 37

11. REFERENCES 38

APPENDIX A. DISTRESS SURVEY WRITTEN LOG A-1

APPENDIX B. DETAILS OF ANALYSIS B-1

LIST OF FIGURES

Figure Page
1 Instrumentation Layout 2
2 Thin Tack Coat of Straight PG 64-22 on Top of Concrete Slabs 3
3 EG Installation on Top of Each Lift 4
4 Overlay Construction 5
5 Overlay Bottom Temperature During Construction Day-1 (April 31st, 2019) 6
6 Overlay Bottom Temperature During Construction Day-2 (May 1st, 2019) 6
7 Bottom EG Responses During North Side Lift-1 Construction (Day-1, April 31st, 2019) 7
8 Bottom EG Responses During South Side Lift-1 Construction (Day-1, April 31st, 2019) 8
9 Mid-depth EG Responses During North Side Lift-2 Construction (Day-2, May 1st, 2019) 8
10 Mid-depth EG Responses During South Side Lift-2 Construction (Day-2, May 1st, 2019) 9
11 Temperature Readings from the South Section 10
12 Strain Responses from the South Section 11
13 Insulation of AC Overlay 12
14 Overlay Temperature Profiles 13
15 Distress Survey Crack Map 14
16 Transverse Reflection Cracks on the Surface 16
17 Cracks on Outer edge of North and South Section 17
18 Cracks on Inner edge of North and South Section. 18
19 Crack Channeling and Isolation Zone 19
20 Overlay Core from Uncracked Area 19
21 Load Cell Readings 20
22 Flow Chart of Damage Analysis 21
23 Tensile Strain Distribution from the 1st Loading cycle 21
24 Determination of *IF*, SG3-N-5 22
25 Failure Strain vs. Depth 23
26 Crack Sequence Contour 24
27 Strain Energy 26
28 Calculation of Fracture Energy 27
29 Fracture Energy 28
30 Crack Propagation Rate vs. Strain Energy Release (Detailed calculations are summarized in table 3 of Appendix B) 30
31 Crack Propagation Rate vs. Fracture Energy Release (Detailed calculations are summarized in table 4 of Appendix B) 30
32 Peak Strain Response in SG3-N-5 31
33 Average Percent Increase in Strain Response at Different Depths (Detailed calculations are summarized in table 5 of Appendix B) 32
34 Viscoelastic Behavior of AC Materials under the effect of (a) Temperature and (b) Loading rate32
35 Strain Energy Preceding, During, and Succeeding the 1st set of Extreme Cooling Cycles 33
36 Fracture Energy Preceding, During, and Succeeding Extreme Cooling Cycles 34
37 Percentage Change in Fracture Energy 35
38 Crack Length vs. Cycle Number 37

LIST OF TABLES

Table	Page
1 Summary of Field Density	5
2 Distress Survey Written Log	15
3 Summary of Cycle Number and Failure Strain at IF	22
4 Summary of Crack Length and Cycle Number	29
5 Summary of Step 1 and 2 Implementation	36

LIST OF ACRONYMS

AC	Asphalt Concrete
EG	Embedded Asphalt Strain Gages
FAA	Federal Aviation Administration
FEM	Finite Element Model
JDG	Joint Displacement Gages
LVDT	Linear Variable Differential Transformers
NAPTF	National Airport Pavement Test Facility
PCC	Portland Cement Concrete
POT	Potentiometers
RCIP-VI	Reflective Cracking Indoor Phase VI
SG	Surface Strain Gages
T	Thermocouples
TESS	Temperature Effect Simulation System

EXECUTIVE SUMMARY

Reflection cracking possesses a major challenge in terms of rehabilitation and repair in airfield pavements. For an asphalt concrete (AC) overlaid rigid pavement, a large daily cooling rate combined with a very low temperature at the end of the cooling cycle represents the most critical condition with respect to the development of thermal induced reflection cracking. However, this distress mode is not addressed in the current Federal Aviation Administration (FAA) advisory circular.

The main focus of Reflective Cracking Indoor Phase VI (RCIP-VI) test was to assess the impact of extreme cooling cycle on the asphalt overlay reflective cracking. Phase VI test overlay is comprised of two 30- by 5-ft overlay strips constructed with the FAA standard P-401 HMA (PG 64-22). The Temperature Effect Simulation System (TESS) was employed to mechanically simulate daily temperature variations. While keeping the maximum joint opening at 12 mil, a higher horizontal opening rate was introduced during the extreme cooling cycles. Key instrumentation included asphalt strain gages and thermocouples at multiple depths in the overlay.

In general, the observations from RCIP-VI test, such as strain distribution, crack initiation sequencing, failure strain at different depths, and crack evolution agreed with the previous experiments. A pronounced effect of extreme cooling cycles on the evolution of reflection cracks was found in the strain response and multi-scale damage analysis. To characterize the crack propagation, a modified Paris and Erdogan Law was proposed based on the release of Strain Energy as well as Fracture Energy.

1. INTRODUCTION

The magnitude of thermal stresses developed in the asphalt concrete (AC) overlay is not generally associated with the seasonal variations (slow changes in temperature) due to the ability of the AC to relax under slow loading conditions. It is the daily temperature change that has the greatest influence on the performance of AC overlay. A large daily cooling rate combined with a very low temperature at the end of the cooling cycle represents the most critical condition with respect to the development of reflective cracking due to horizontal slab movement, as well as low temperatures causing the HMA overlay to stiffen (the stiffer the AC, the less likely it will relax under straining, resulting in the development of a crack (1-3).

1.1 OBJECTIVES

The primary objective of Reflective Cracking Indoor Phase-VI (RCIP-VI) test was to assess the effect of extreme cooling cycles on the crack evolution through varied displacement rates. Secondly, it was expected to obtain the model parameters of Paris and Erdogan Law from full-scale test data to support the parallel modeling effort on the crack propagation.

1.2 TEST OVERLAY AND INSTRUMENTATION

To maintain consistency from the previous experiments, Phase VI test overlay included two strips that were 30- by 5-ft with a 2 ft. space in between. Both 5-in thick sections were constructed with the same materials in accordance with the Federal Aviation Administration (FAA) standard P-401 HMA (PG 64-22). To capture and quantify crack initiation and propagation, instrumentation was designed to acquire, but not limited to, joint displacement, overlay temperature profile, and strain responses at different overlay depths. Instrumentation took place in three stages: pre-construction, during construction, and post-construction. To facilitate instrumentation, the overlay was placed in two 2.5-in lifts. Prior to the overlay construction, six potentiometers (POT), four linear variable differential transformers (LVDT), and four joint displacement gages (JDG) were connected and secured. The purpose of these sensors was to monitor the performance of the Temperature Effect Simulation System (TESS). During the overlay paving, eight H-type embedded asphalt strain gages (EG) were installed at the bottom of each overlay lift (2.5 in.). After the paving, twenty surface strain gages (SG) were installed at various locations on the surface. Two thermocouple trees were installed in the overlay and each tree contained multiple thermocouples (T) to measure the temperature at the same depth as the strain gages. A detailed instrumentation layout is shown in Figure1. Note that all strain gages were placed directly above and perpendicular to the concrete joint where the reflection crack would be expected.

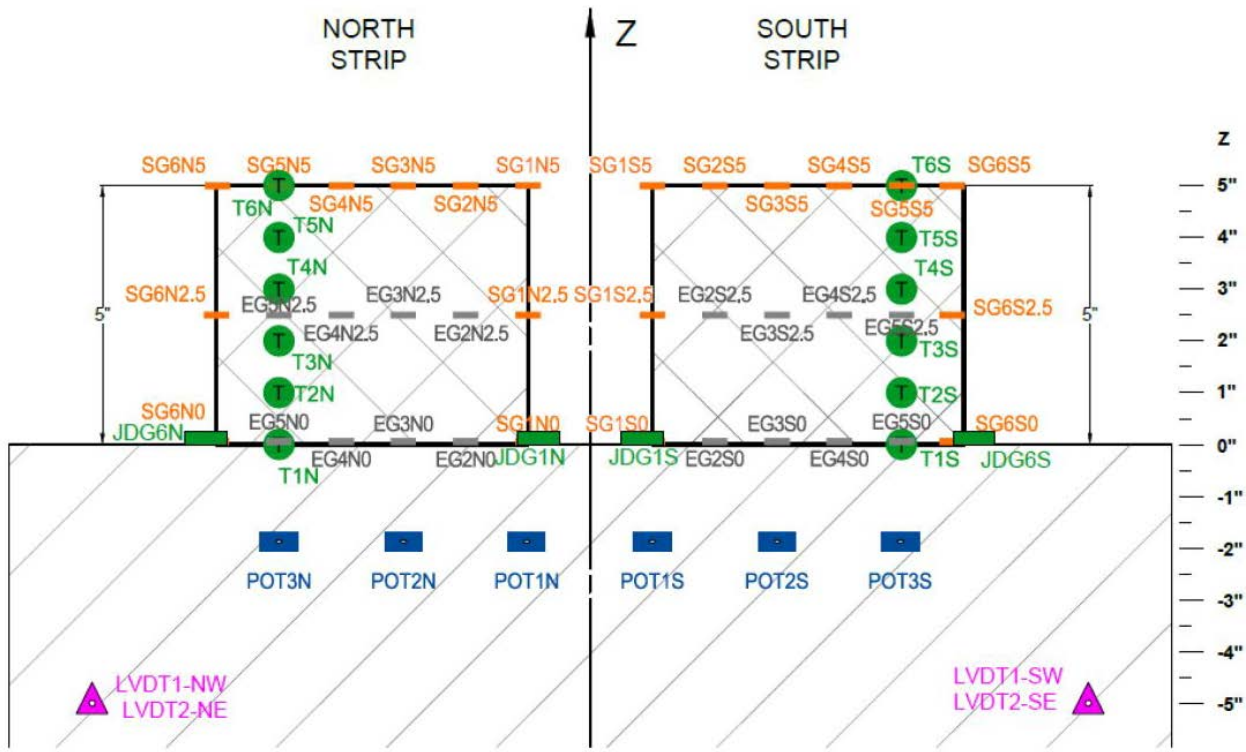

INSTRUMENT KEY						
	EG	EMBEDDED DYNATEST STRAIN GAGE			LVDT	LINEAR VARIABLE DISPLACEMENT TRANSDUCER
	JDG	JOINT DISPLACEMENT GAGE			SG	SURFACE STRAIN GAGE
	POT	POTENTIOMETER			T	THERMOCOUPLE

Figure1. Instrumentation Layout

2. OVERLAY CONSTRUCTION

Prior to the overlay construction, the milled concrete slab surface was thoroughly swept to remove all loose dirt and debris. To prevent interface slippage and secondary cracks, a thin tack coat of straight PG 64-22 binder was applied to the dry surface of two 12-in.-thick, 15- by 15-ft concrete slabs as shown in Figure2. The surface was then allowed to cure without being disturbed for the period of time necessary to permit drying and setting. Prior to the overlay paving, H-type asphalt strain gages (EG) were first secured atop concrete slabs using straight PG 64-22 asphalt binder (Figure3(a)). These gages were then covered by loose FAA standard P-401 HMA materials close to the lift thickness (Figure3(b)) and the screed of the paver was used to strike off the excess HMA to the proper depth and grade.

On April 30, 2019, the placement of the first lift started on the south section around 11:00 AM and the north section paving took place an hour later. The second lift was placed on the next day (May 1, 2019). The paving of south section started around 9:30 AM and the north section paving took place an hour later.

Figure2. Thin Tack Coat of Straight PG 64-22 on Top of Concrete Slabs

(a)

(b)

Figure3. EG Installation on Top of Each Lift

Figure4 shows the complete test overlay after construction. After placing each lift, the HMA materials were thoroughly and uniformly compacted by a power roller without vibration due to the sensors underneath. Then the density atop each lift was measured using Nuclear Densometer at a minimum of four locations on each section (north and south). The density results are presented in Table 1 and the average was about 92%.

Figure5 shows the thermocouple readings (T1S & T1N) from the first day of paving of the 1st lift (April 30th, 2019) and Figure6 shows the thermocouple readings (T1S & T1N) from the second day of paving of the 2nd lift (May 1st, 2019). As shown in Figure5 and Figure6, the thermocouple readings atop concrete slabs clearly registered the placement of each lift and cool down progression.

Figure4. Overlay Construction

Table 1. Summary of Field Density

Overlay Section	Lift	Field Density, %	Roller Passes
North	1st	92.4	8
North	2nd	91.3	8
South	1st	92.3	8
South	2nd	92.0	8

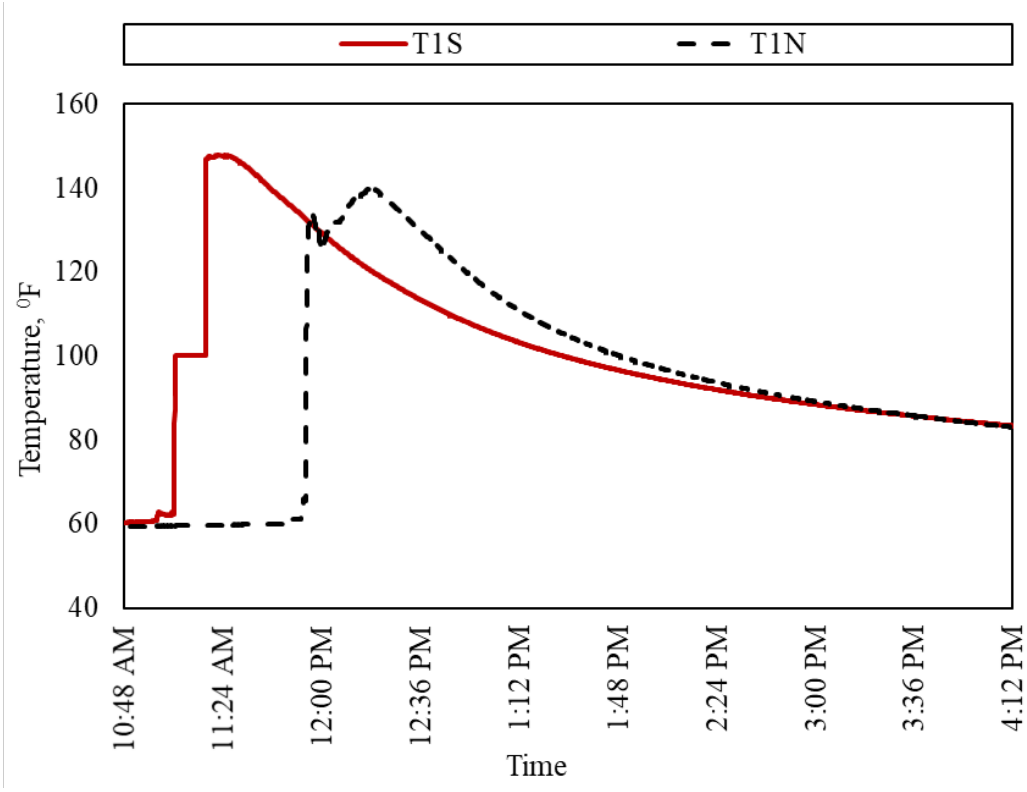

Figure5. Overlay Bottom Temperature During Construction Day-1 (April 31st, 2019)

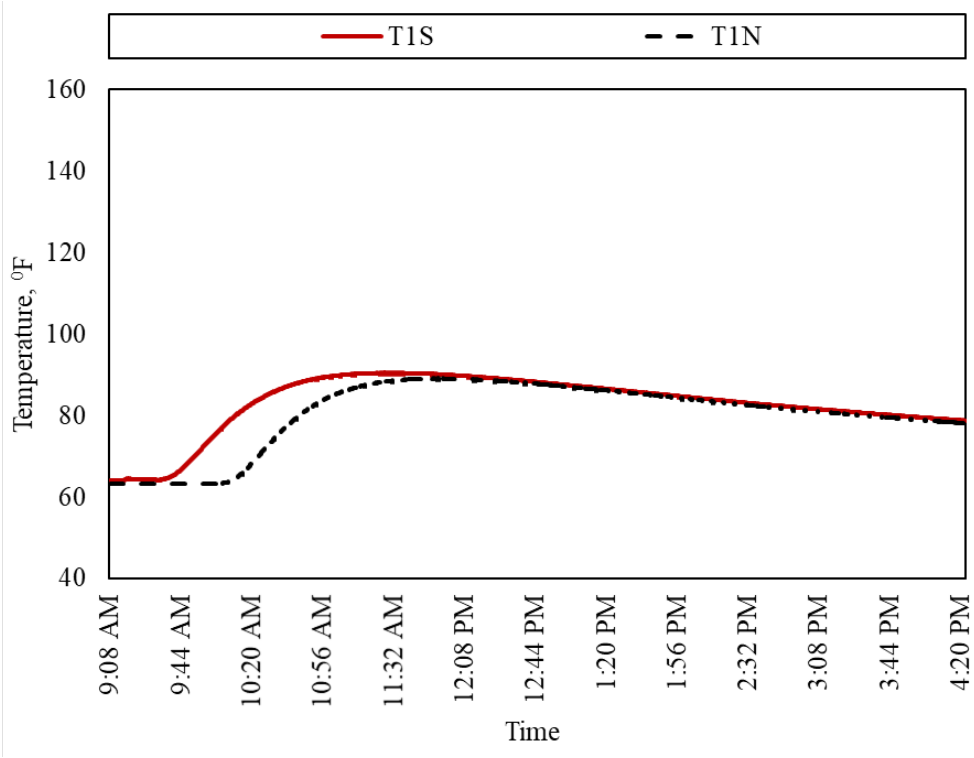

Figure6. Overlay Bottom Temperature During Construction Day-2 (May 1st, 2019)

Sample bottom EG responses during the paving of 1st lift of north and south section are presented in Figure7 and Figure8, respectively. A cluster of peak strains were observed among the EG during the occurrence of material lay down and roller compaction. After the compaction, similar strain magnitudes were seen in both north and south sections. Sample mid-depth EG responses during paving of 2nd lift of north and south section are presented in Figure9 and Figure10, respectively. Similar to the bottom EG, good construction quality as well as repeatability of the sensors were observed.

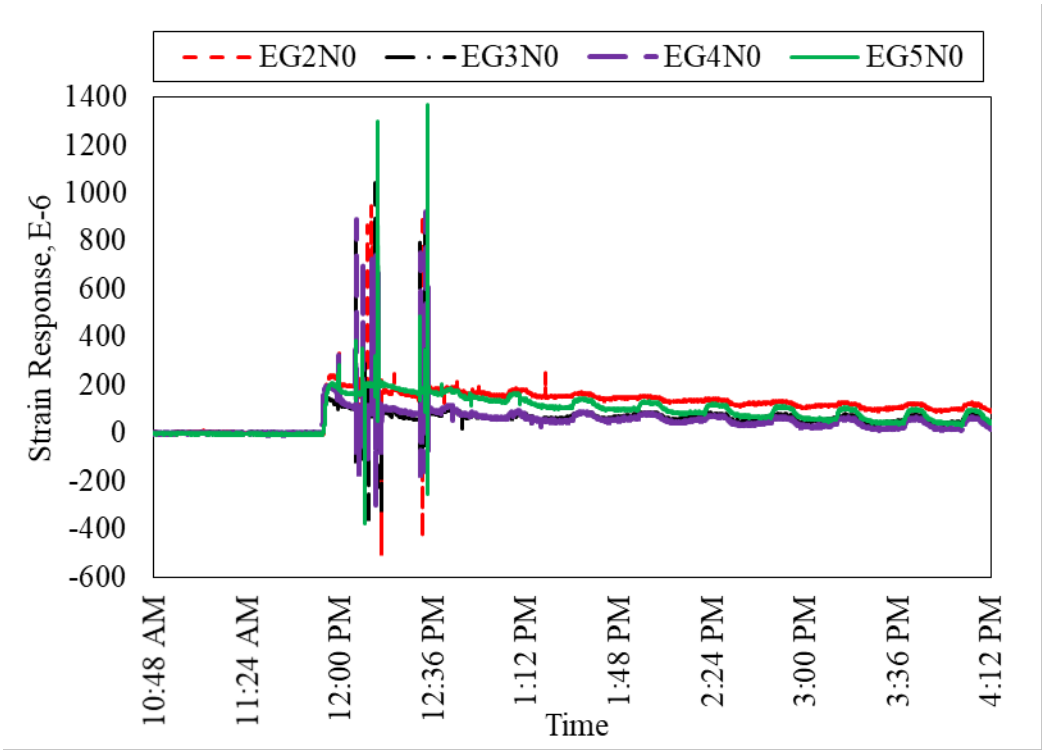

Figure7. Bottom EG Responses During North Side Lift-1 Construction (Day-1, April 31st, 2019)

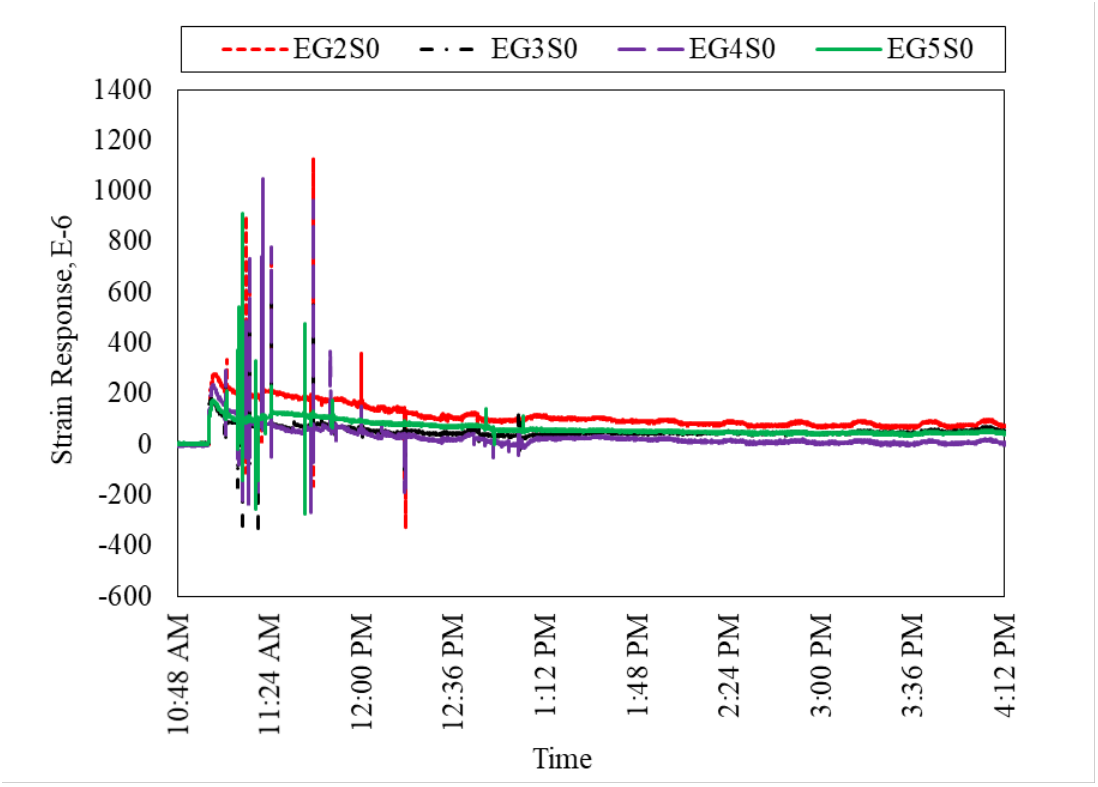

Figure8. Bottom EG Responses During South Side Lift-1 Construction (Day-1, April 31st, 2019)

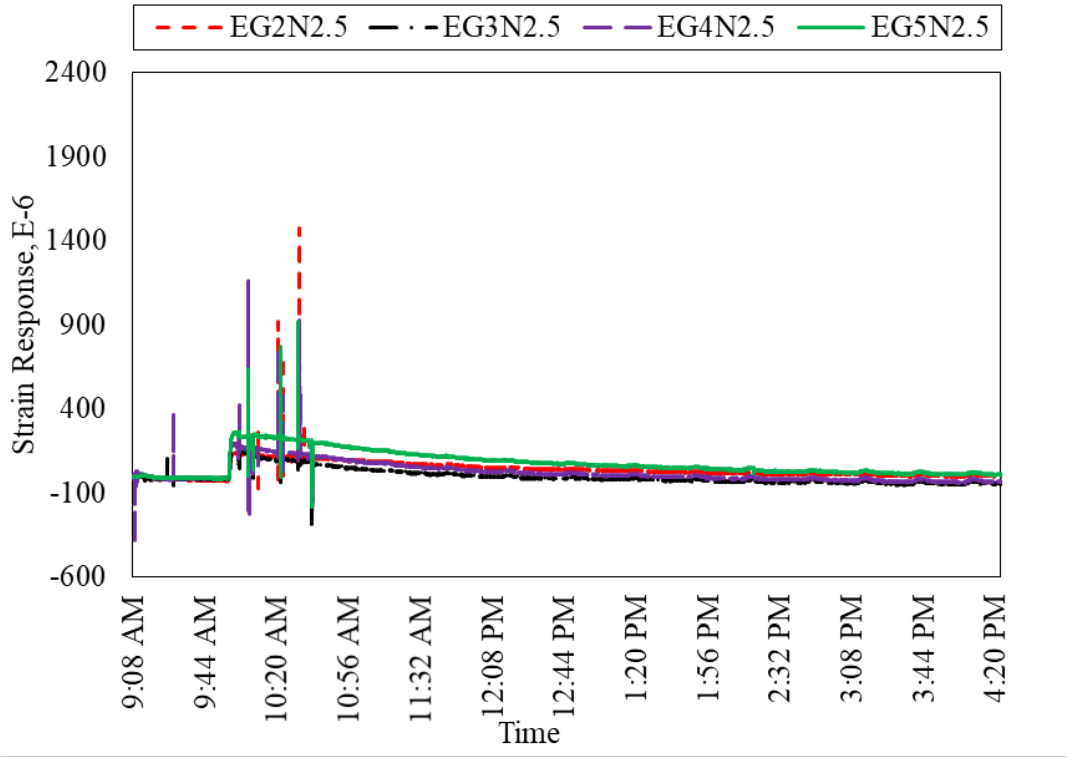

Figure9. Mid-depth EG Responses During North Side Lift-2 Construction (Day-2, May 1st, 2019)

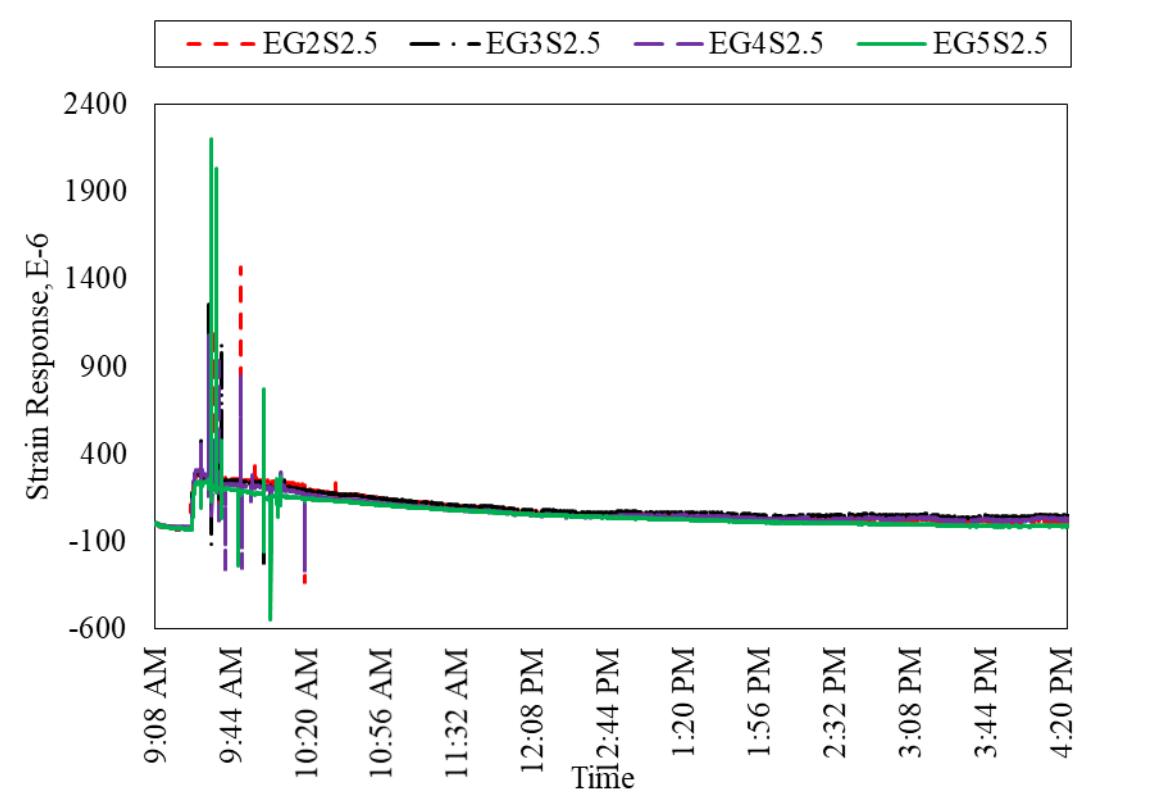

Figure10. Mid-depth EG Responses During South Side Lift-2 Construction (Day-2, May 1st, 2019)

3. SHAKE-DOWN TEST

To ensure the functionality of the TESS, instrumentation, and data acquisition system, a total of 100 cycles were executed. Temperature variations were approximated by a haversine waveform describing the relationship between the joint opening, *d(t)*, and cycle time:

$$d(t) = D\sin^2\left(\frac{\pi}{2} + \frac{\pi t}{T}\right) + R \tag{1}$$

where t is the time, D is the amplitude of joint opening, T is the cycle time, and R is the rest period at the end of each loading cycle. For the 100-cycle shake-down test, each loading cycle comprised of a loading time of 75 seconds, unloading time of 75 seconds, and rest period of 600 seconds to allow for sufficient relaxation of AC materials. Thejoint opening was set to 5 mil. For demonstration purposes, temperature readings from the south section are shown in Figure11. A uniform temperature at different depths was maintained. Sample strain gage responses at the overlay bottom, mid-depth and surface from the south section are shown in Figure12. As expected, strains at the bottom were the highest. There was a gradual decrease of the bottom strains, which was due to the initial stretch of the overlay, and the strain values became constant afterwards.

At the end of shake-down test, the overlay was thoroughly inspected for damage and no visible cracks were observed. All instrumentation sensors and the data acquisition system were fully functional.

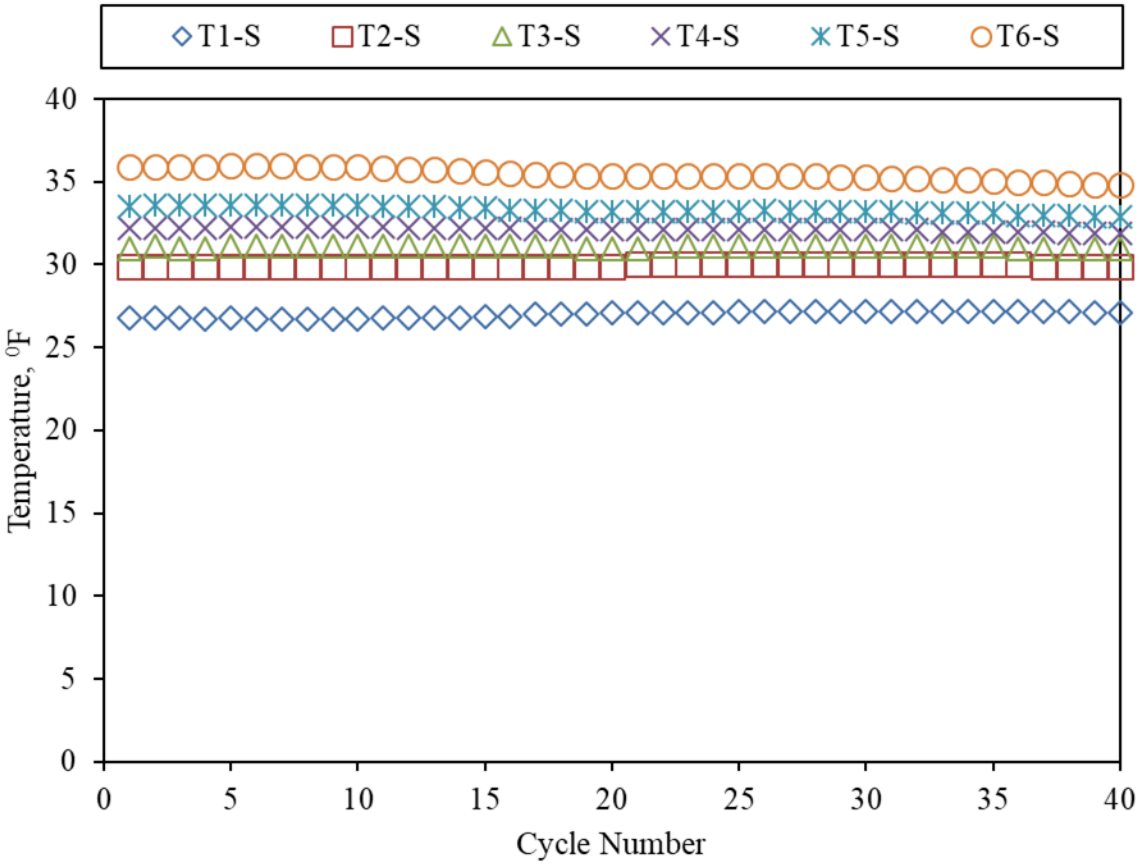

Figure11. Temperature Readings from the South Section

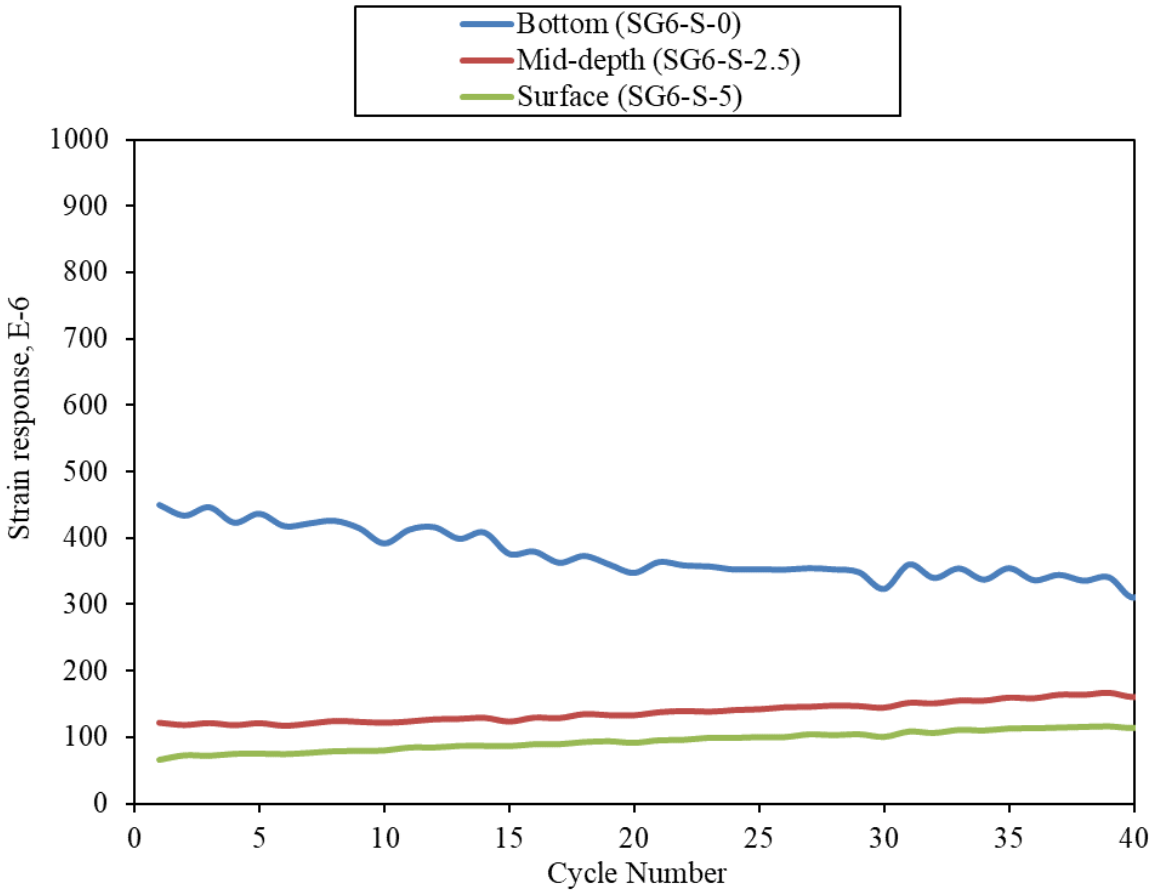

Figure12. Strain Responses from the South Section

4. FORMAL TEST

Formal RCIP-VI testing started on June 7, 2019. The 360-day temperature variations with extreme cool cycles were simulated in two steps. For the first 330 loading cycles, each cycle began with a loading time of 75 seconds. Once the actuators (north and south) reached the maximum horizontal displacement (joint opening) of 12 mil, a 75 second unloading was executed, followed by a rest period of 600 seconds to allow the overlay to relax. Then, a different test recipe was executed for the next 30 loading cycles with the same maximum displacement (12 mil). But both the loading and unloading time was shortened to 35 seconds. For these 30 loading cycles, a rest period of 300 seconds was also included (4). The TESS was programmed to maintain a target temperature of 33^0F at the AC – portland cement concrete (PCC) interface. Insulation blankets were used on the pavement surface to maintain the overlay temperature (Figure13). There was a power outage at the FAA National Airport Pavement Test Facility (NAPTF) on June 16, 2019. Therefore, instrumentation data between Cycle Number 833 and 1150 was not available.

Figure13. Insulation of AC Overlay

4.1 TEMPERATURE CONTROL

Three sets of thermocouple readings at different overlay depths are presented in Figure14. Through the course of testing, the overlay maintained a relative uniform temperature (less gradient). Towards the end of testing (i.e., Cycle-6426), the temperature in the top portion of the overlay raised due to the increasing ambient temperature in the NAPTF.

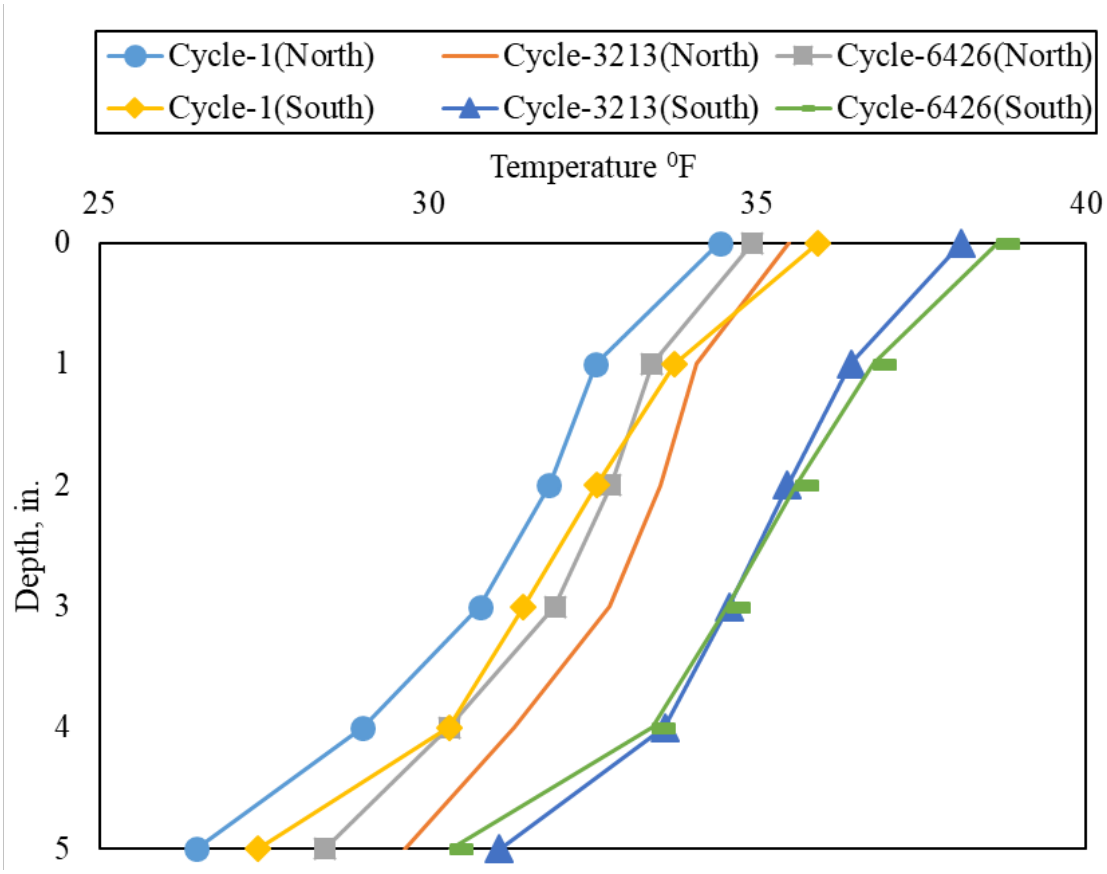

Figure14. Overlay Temperature Profiles

4.2 PERFORMANCE MONITORING

Distress surveys were conducted multiple times a day. All identified cracks were outlined with chalk when needed and measured using a tape measure. Any changes to existing cracks were recorded along with any new cracks. Results of the visual distress survey were documented in two ways: a scale map and a written log. The map displays all cracks on a scaled drawing. Figure15 provides a small sample of the distress map. The distresses were numbered for reference to the written log. The written log provides all the crack information chronologically. Table 2 provides a sample of the distress map written log. The written log documents the date of entry, the cycle number, the type of cracks, the crack number – which can be referenced to the distress map, the location of crack and length, and any relevant notes. The notes would indicate any changes to existing crack, merging of multiple previously identified cracks, and so on. A complete written log is provided in Appendix A.

Color	Date	Total Cycles
	6/10/2019	320
	6/11/2019	480
	6/12/2019	565
	6/12/2019	595
	6/13/2019	680

	6/13/2019	725
	6/14/2019	800
	6/17/2019	1160
	6/18/2019	1284
	6/19/2019	1388
	6/20/2019	1515
	6/21/2019	1630
	6/24/2019	1724
	6/27/2019	2100
	7/1/2019	2550
	7/3/2019	2820
	7/8/2019	3200
	7/16/2019	4015

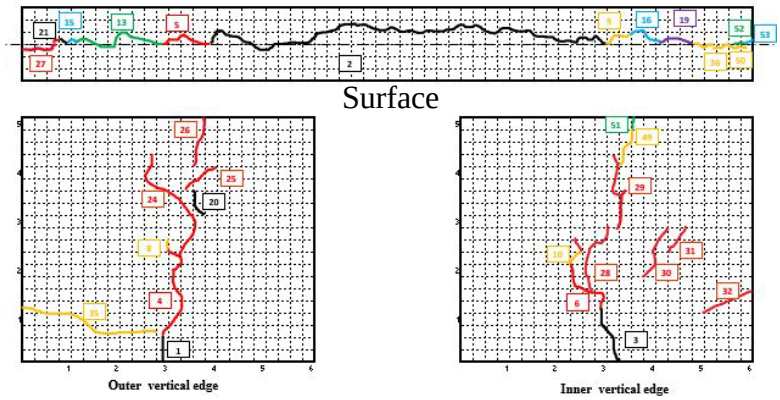

(a) North

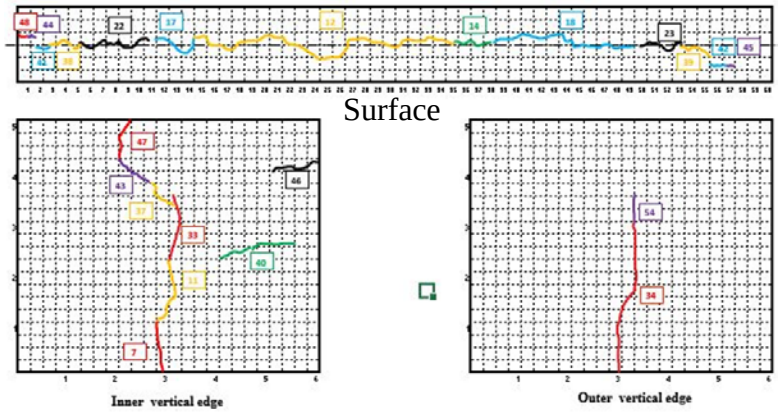

(b) South

Figure15. Distress Survey Crack Map

Table 2. Distress Survey Written Log

Date	Total Cycles		Daily Cycles	Distress						
				Description	No.	Location				
						X Axis (in.)		Y Axis (in.)		Location
	North	South				Initial	End	Initial	End	
6/10/2019	320	320	120	Bottom-up crack	1	2.875	2.875	0	1.125	Outer vertical edge, North
6/10/2019	320	320	120	Transverse surface crack	2	16	47.5	2.5	4.625	North section
6/10/2019	320	320	120	Bottom-up crack	3	2.875	3.125	0	1.125	Inner vertical edge, North
6/11/2019	480	480	120	Bottom-up crack	4	2.875	3.25	1.125	2.25	Outer vertical edge, North
6/11/2019	480	480	120	Transverse surface crack	5	11.5	16	3	3.62	North section
6/11/2019	480	480	120	Bottom-up crack	6	2.25	2.875	1.125	2	Inner vertical edge, North

4.3 OBSERVATIONS

Reflection cracks initiated from the overlay bottom and propagated to the surface. Bottom-up cracks were first observed on the outer edge of the north section followed by the inner edge. Similar observations were obtained from the south section but after more loading cycles. After 6426 loading cycles, RCIP-VI testing concluded on August 5, 2019. Directly above the underlying PCC joint, continuous transverse reflection cracks were observed on the overlay surface (Figure16(a) and (b)). Pictures of the final stage of vertical edges are provided in figures 17 and 18. Three of four edges showed full-depth reflection cracks except for the outer edge of the south section (Figure17 (b)). The uncracked area was most likely due to an isolation zone caused by mixed-mode fracture under crack channeling. As illustrated in Figure19, when a Mode I crack formed and developed to a critical length, a mixed-mode fracture occurred and led the crack to advance in other orientations (4). Later, a 4-in diameter overlay core was taken from the uncracked area and confirmed no visible cracks (Figure20).

(a) North

(b) South

Figure16. Transverse Reflection Cracks on the Surface

(a) North

(b) South

Figure17. Cracks on Outer edge of North and South Section

(a) North

(b) South

Figure18. Cracks on Inner edge of North and South Section.

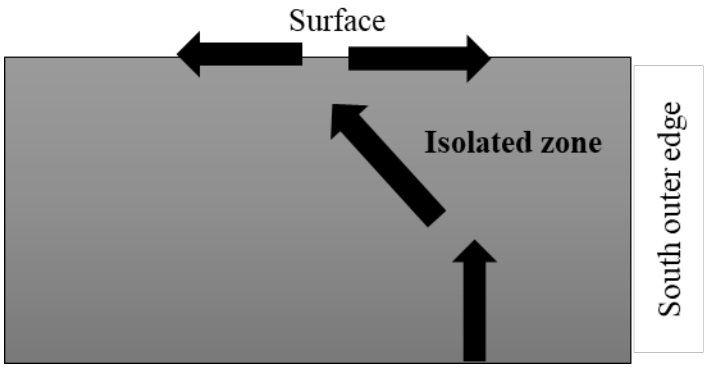

Figure19. Crack Channeling and Isolation Zone

Figure20. Overlay Core from Uncracked Area

5. OVERLAY DETERIORATION

Through the course of full-scale testing, a slight difference in load cell readings was observed between the north and south section during the generation of equal joint displacements along the outer edges. This difference may be attributed to the non-uniform AC-PCC interface conditions from the milling and tack coat application. Figure21 reveals four distinct stages that were also identified in Reflective Cracking Indoor Phase V (RCIP-V) test (5). A rapid load reduction (66 lbs/cycle) was observed in Stage 1. On the vertical edges, bottom-up cracks initiated and started

propagating upwards, as recorded in the distress survey. A noticeable load jump coincided with the 1st set of extreme cooling cycles (331-360 loading cycles). In Stage 2, the load decreased at a slightly lower rate of 50 lbs/cycle. At the end of this stage, both inner and outer edges of the north section were completely cracked. Transverse reflection cracks on the surface became more visible. On the south section, bottom-up cracks reached approximately 3.5 in on the inner and outer edges. Compared to Stage 1, less of a load increase was observed during the 2nd set of extreme cooling cycles (691-720 loading cycles). In Stage 3, a load reduction continued but at a much lower rate (1.35 lbs/cycle). Bottom-up cracks appeared at the surface of the south section. Stage 4 began with a drop of 3,700lbs and maintained steady till the end of testing. Except for the outer edge of the south section, a complete separation of the overlay was observed.

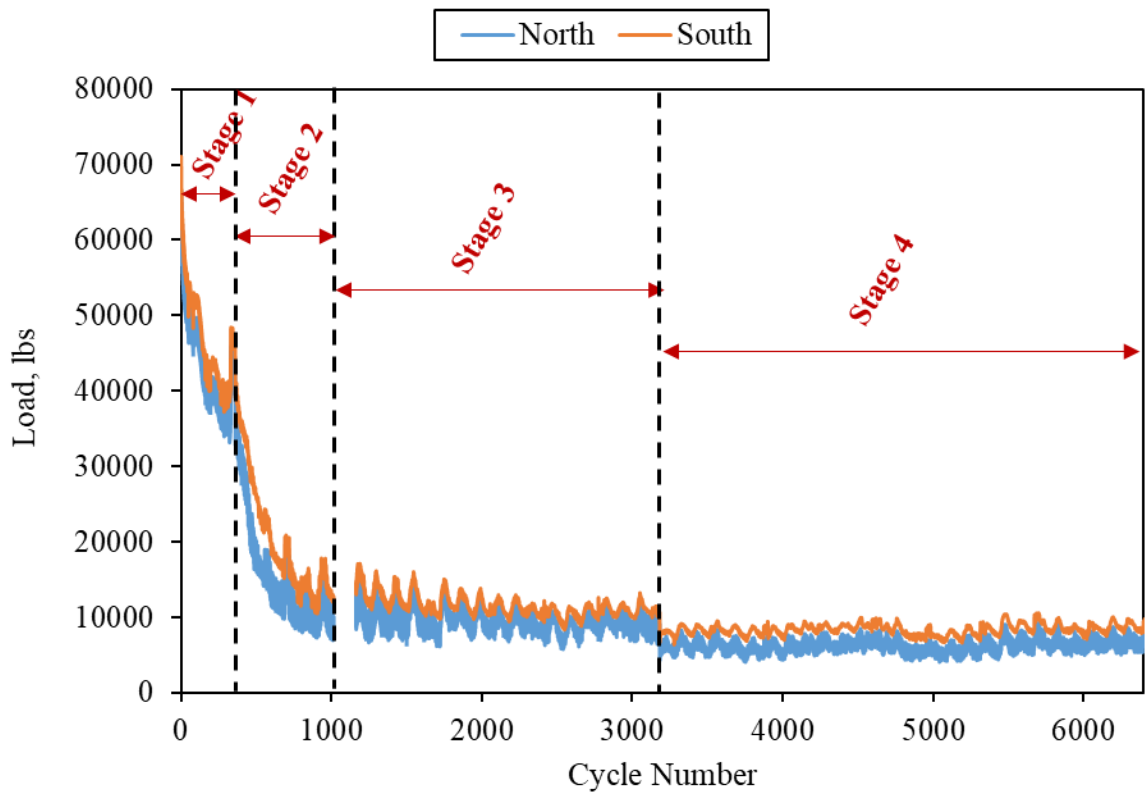

Figure21. Load Cell Readings

6. DAMAGE ANALYSIS

Crack evolution is a multi-scale phenomenon. Cracks develop as micro-cracks at points of stress concentration which coalesce to form macro-cracks. Reflective cracking in an AC overlay is driven by crack nucleation, initiation, and propagation (6). Crack nucleation and crack initiation needs to be conducted on both a micro and macro scale (Figure22). At a micro-scale, failure strain was selected as the damage parameter for crack initiation because it represents localized damage occurring in the vicinity (5). At a macro-scale, strain energy and fracture energy were deemed as the most appropriate parameters.

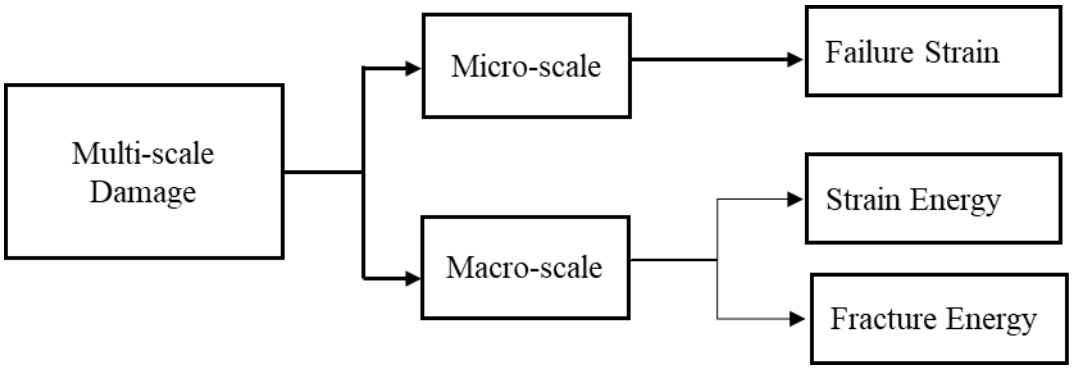

Figure22. Flow Chart of Damage Analysis

6.1 FAILURE STRAIN

Figure23 shows plots of the peak strain responses from the 1st loading cycle in a contour format. Strain responses were tensile in nature and increased with the overlay depth. The highest tensile strains were observed at the bottom outer edges, indicating the initial occurrence of reflection cracks.

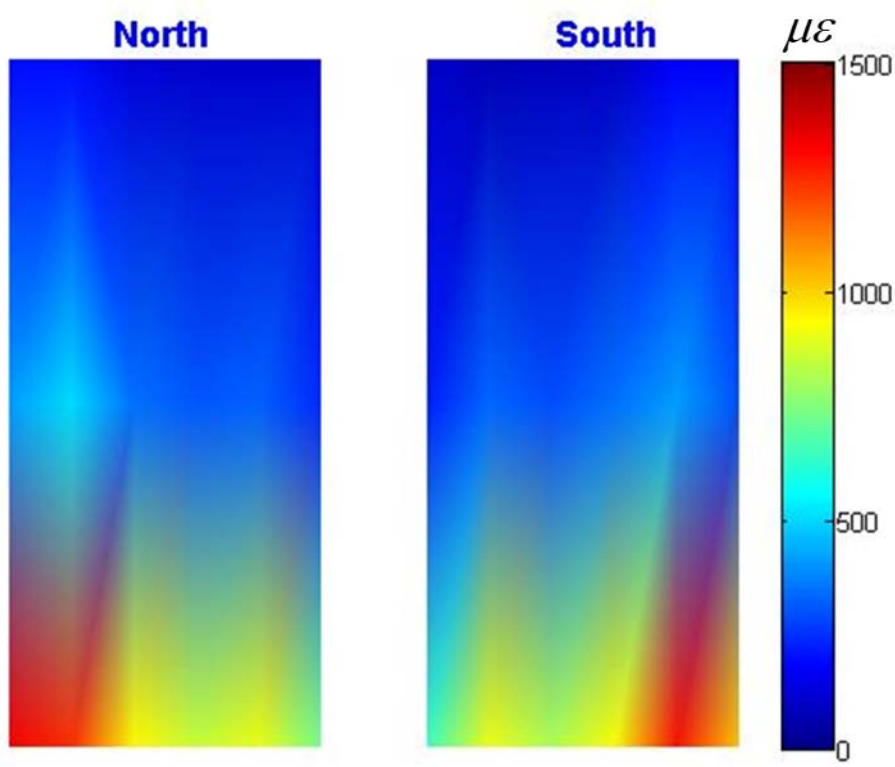

Figure23. Tensile Strain Distribution from the 1st Loading cycle

Following the previous FAA reflective cracking research (4, 5, 7, 8), the inflection point (*IF*) represented the sharp change on the strain response curve under repeated loading. Peak strain corresponding to *IF* was defined as the failure strain. For most of the strain gages, the tangent

method, which is point of intersection of two tangents from initial and the final point, was able to detect the IF (Figure24). In Figure24, conceptually, point (a) would be considered as *IF* (5); however, considering the sharp strain increase during the extreme cooling cycle, point (b) was considered to be the *IF*. The position of point (b) varied from sensor to sensor and engineering judgement was used to determine the exact location. The cycle number and failure strain at the *IF* are summarized in Table 3. Note most embedded strain gages (EG) failed during the NAPTF power outage on June 16, 2019.

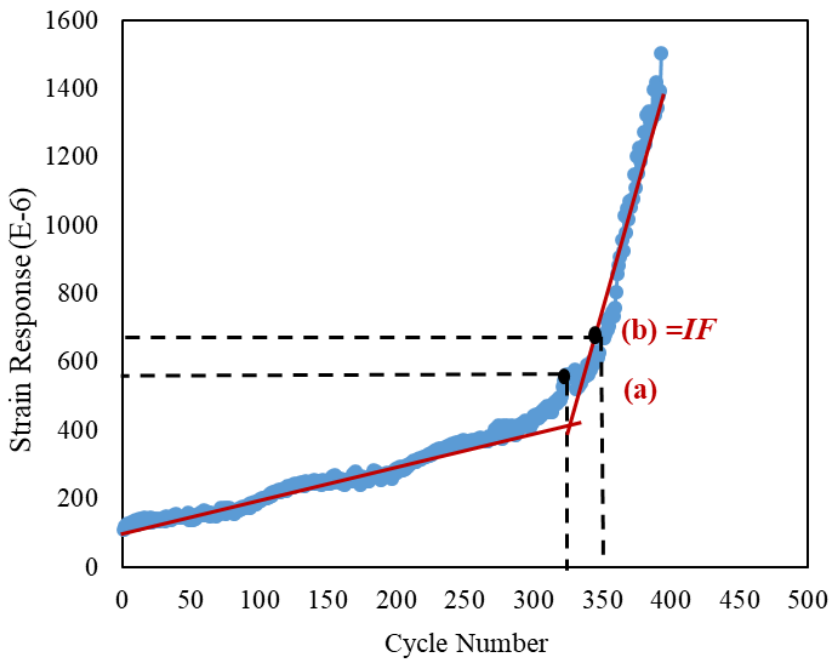

Figure24. Determination of *IF*, SG3-N-5

Table 3. Summary of Cycle Number and Failure Strain at IF

Sensor ID	Cycle Number	Failure strain, E-6	Sensor ID	Cycle Number	Failure Strain, E-6
SG1-N-0.0	251	1169	SG1-S-0.0	380	1194
SG1-N-2.5	487	842	SG1-S-2.5	574	887
SG1-N-5.0	600	417	SG1-S-5.0	700	424
SG2-N-5.0	563	498	SG2-S-5.0	570	400
SG3-N-5.0	350	682	SG3-S-5.0	380	618
SG4-N-5.0	358	686	SG4-S-5.0	525	706
SG5-N-5.0	512	645	SG5-S-5.0	1529	529
SG6-N-5.0	546	498	SG6-S-5.0	-[1]	-[1]
SG6-N-2.5	361	752	SG6-S-2.5	-[2]	-[2]
SG6-N-0.0	84	1378	SG6-S-0.0	250	1110

Note 1: Strain gage did not reach *IF*
Note 2: Strain response data was not recorded due to power outage.

Similar to the previous experiments (Figure18 of (4), Figure20 of (5), and Figure4 of (7)), a strong dependency of failure strains on the overlay depth was observed from RCIP-VI test data, as shown in Figure25. The failure strain decreased in magnitude with crack propagation towards the overlay surface. Average failure strain of north and south sections at the bottom, mid-depth, and surface of the overlay was 1215, 890, and 560 microstrains, respectively.

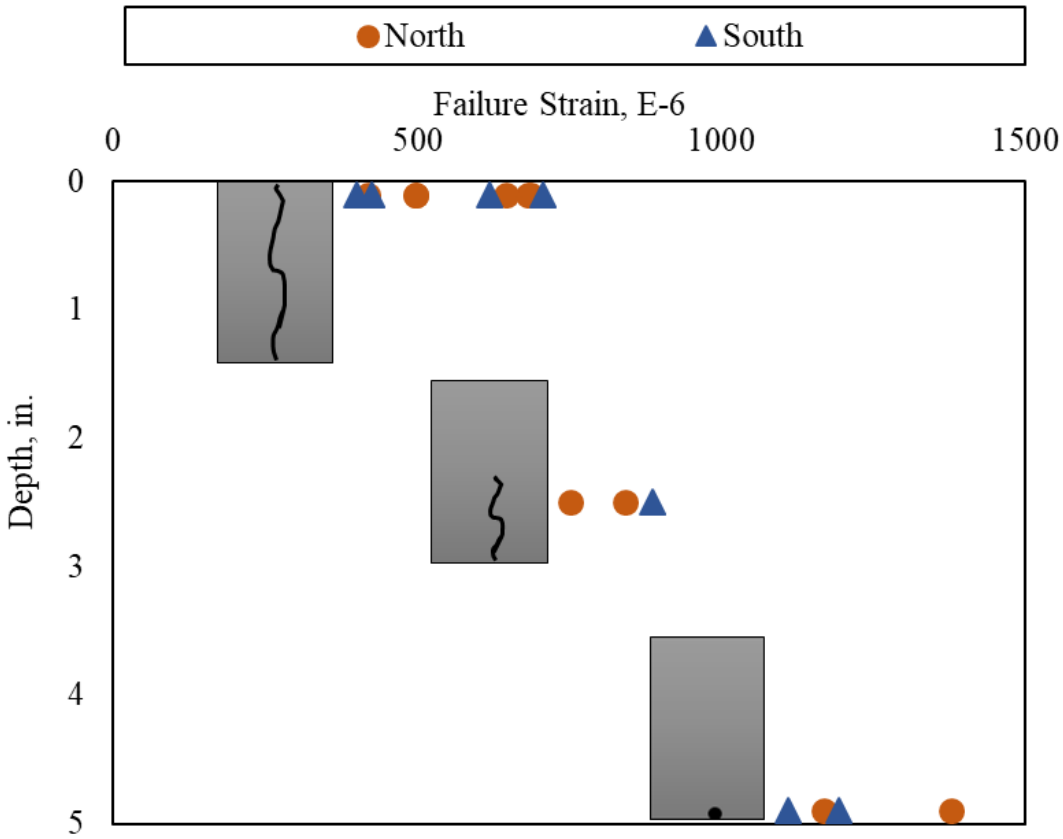

Figure25. Failure Strain vs. Depth

Figure26 shows a contour plot generated by the number of cycles at the *IF* (Table 3). Bottom-up cracks on both north and south sections initiated at the outer edge where the highest stress concentration was expected. Once transverse reflection cracks reached the overlay surface, it progressed to the edges. This crack sequence agreed with the distress survey (Appendix A). Considering the linear propagation along the horizontal and transverse directions, the average crack propagation rate in the horizontal (transverse) direction (CPR_H) for the north section was 0.11 in./cycle whereas for the south section it was 0.075in./cycle. The average crack propagation rate in the vertical direction (CPR_V) for the north and south section was 0.013 and 0.015 in./cycle respectively. RCIP-V test data (Figure23 of (5)) also concluded that CPR_H was much higher compared to CPR_V. Calculation details of CPR are reported in table 1 of Appendix B.

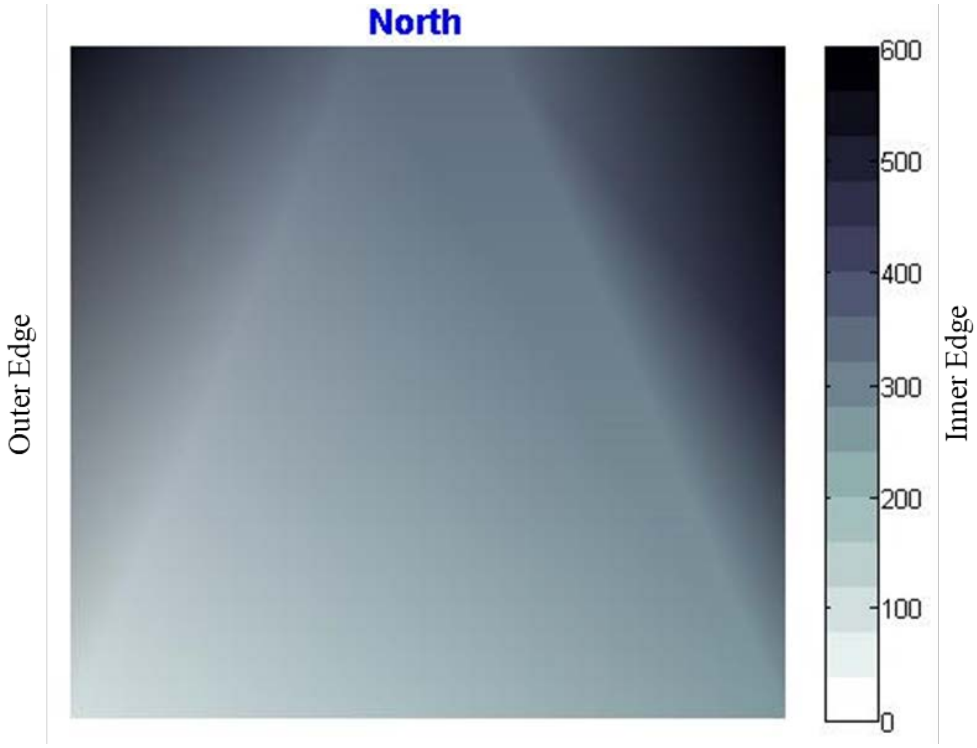

(a) North

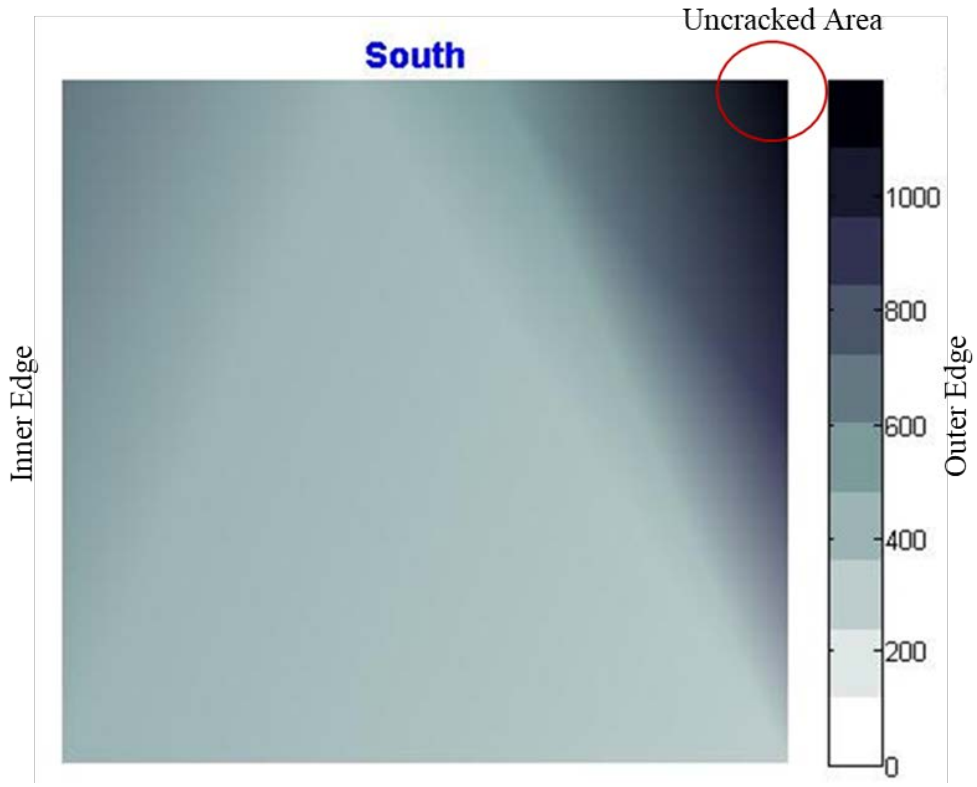

(b) South

Figure26. Crack Sequence Contour

6.2 STRAIN ENERGY

Strain Energy is defined as elastic energy stored in the body under loading (9-11). From the basic principles of work and energy, strain energy density $\left(U^{'}\right)$ is defined as:

$$U^{'} = \frac{1}{2}\sigma\varepsilon \tag{2}$$

where σ is the stress and ε is the strain. Internal Strain Energy per unit area in the undamaged system $\left(U_{Undamaged}\right)$ can be defined as:

$$U_{Undamaged} = \frac{1}{2}\sigma\varepsilon d \tag{3}$$

where d is the depth of an undamaged overlay system with zero crack length. Considering unit area, internal Strain Energy associated with a damaged system is given by Equation 4.

$$U_{Damaged} = \frac{1}{2}\sigma\varepsilon\left(d^{'}\right) \tag{4}$$

where $d^{'}$ is the effective depth. Internal Strain Energy is reduced as a result of crack propagation. From the RCIP-VI test data, $U_{Undamaged}$ and $U_{Damaged}$ were determined as follows:

1. Calculate the average peak strain from bottom, mid-depth, and top gage responses for each loading cycle till the inflection point of the respective gage (for demonstration purpose, calculations for cycle 1 and 361 are shown in table 2 (a) of Appendix B).
2. Calculate the stress from the peak load (from load cell readings) and cross-sectional area for each loading cycle (see table 2 (b) of Appendix B).
3. Calculate $U_{Undamaged}$ and $U_{Damaged}$ using Equations 3 and 4 (see table 2 (c) of Appendix B).

Figure27 demonstrates $U_{Undamaged}$ and $U_{Damaged}$ for the north section, and both followed an identical path until the crack initiation. Strain Energy at crack initiation was defined as Critical Strain Energy. During the crack propagation, $U_{Undamaged}$ and $U_{Damaged}$ gradually deviated but continued to decay in a linear pattern until the crack reached the mid-depth of overlay. Once the crack penetrated into the upper portion of the overlay, both $U_{Undamaged}$ and $U_{Damaged}$ decreased more rapidly due to the strain energy release (3).

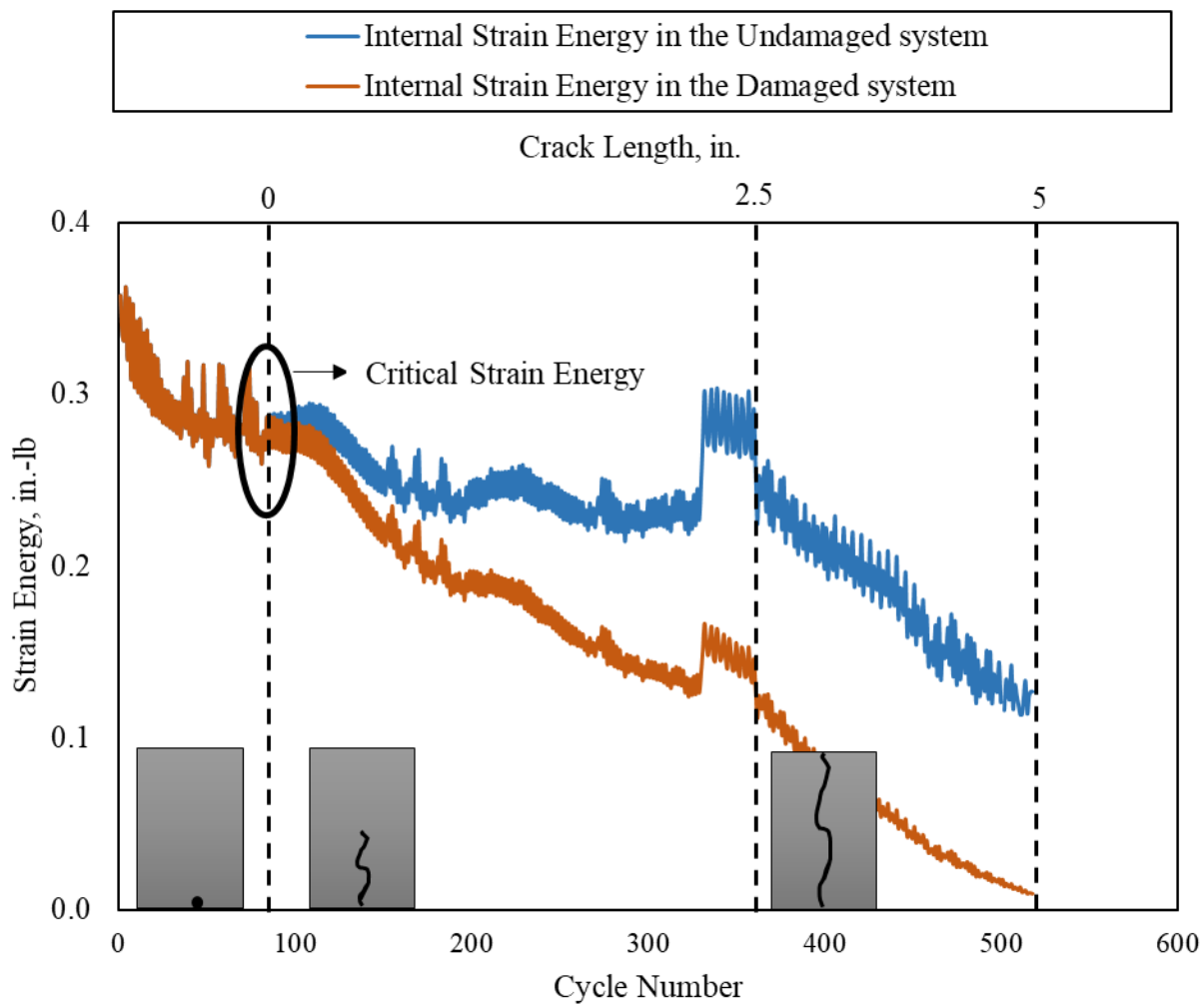

Figure27. Strain Energy

6.3 FRACTURE ENERGY

Fracture Energy (G) is defined as the area under the loading regime on the load vs. displacement curve, as illustrated in Figure28 (12, 13). To separate the two phases of crack formation, initiation and propagation, Equation 11 of RCIP-IV Comprehensive Report (7) was adopted to determine the number of cycles for crack initiation:

$$N_{ini} = d_1 \left(N_f \right)^{d_2} \tag{5}$$

Model coefficients d_1 and d_2 were assumed to be 0.355 and 0.961 (7), respectively. Given N_f was 700 for RCIP-VI test data, N_{ini} was found to be 192.

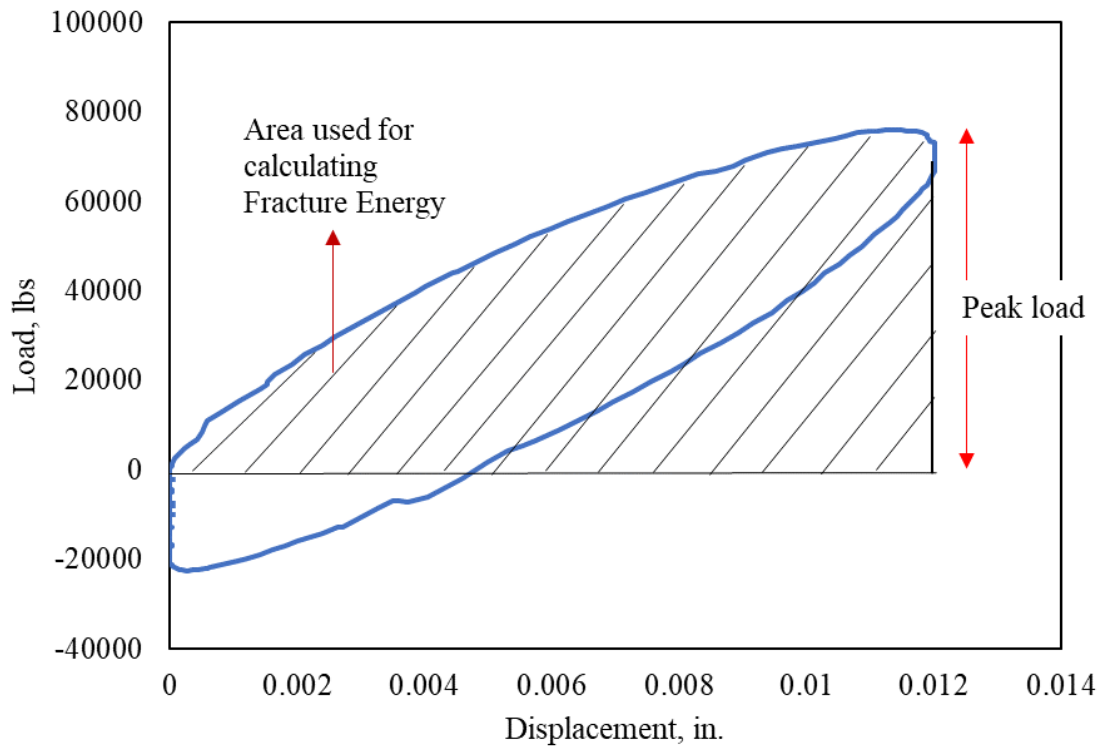

Figure28. Calculation of Fracture Energy

Fracture Energy of each loading cycle in the crack initiation stage (Cycle 1 to Cycle 192) and propagation stage (Cycle 193 to Cycle 2700) is provided in Figure29. Fracture Energy at crack initiation was defined as Critical Fracture Energy. Due to the overlay deterioration, less and less energy was required to maintain the joint opening of 12 mils till Cycle 925. Afterwards, the Fracture Energy remained steady with the progression of loading cycles, indicating a completion of crack propagation in the overlay.

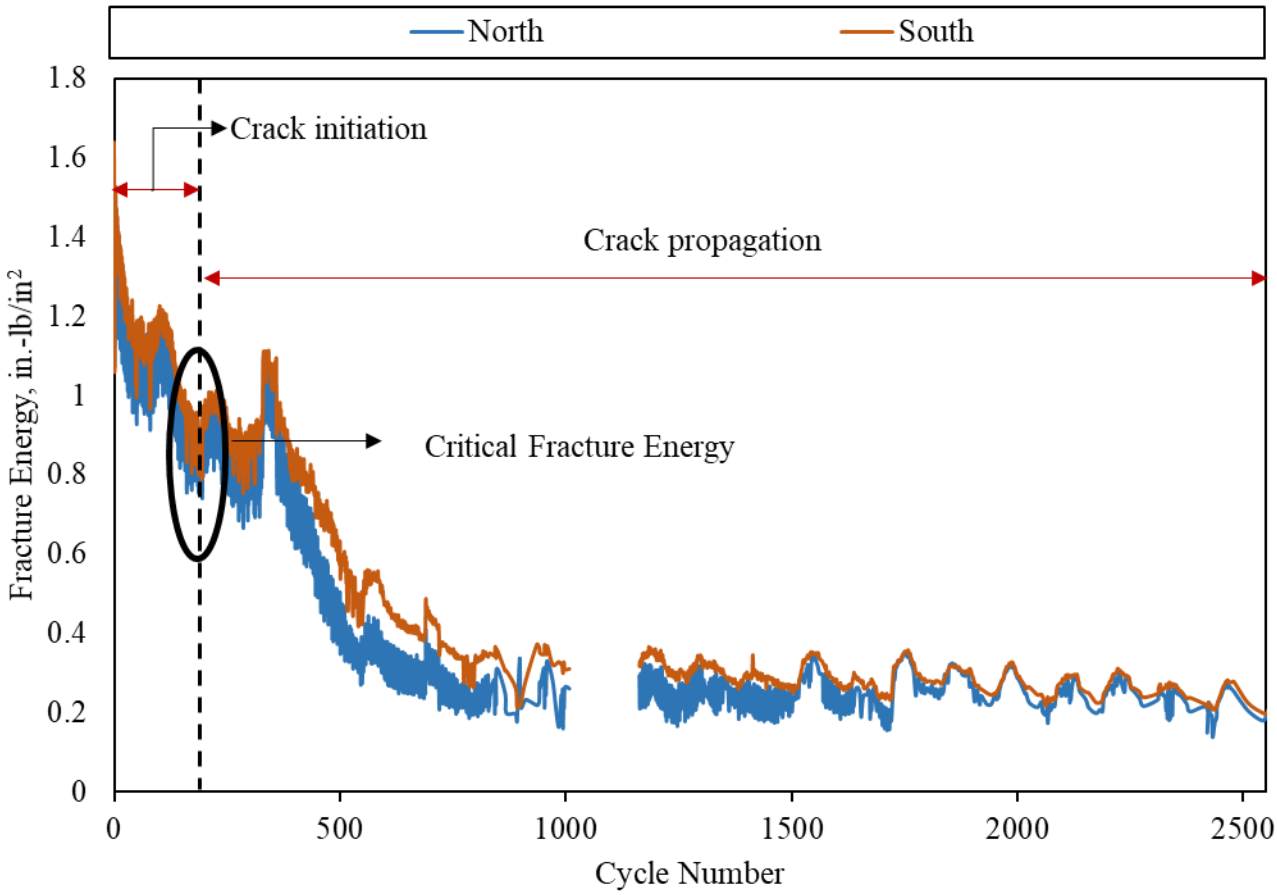

Figure29. Fracture Energy

7. CRACK PROPAGATION ANALYSIS

Paris and Erdogan Law (14) has been used extensively for modelling crack propagation in linear elastic materials (3, 15-20). It relates the crack growth rate to the stress intensity factor (SIF) and is given by:

$$\left(\frac{da}{dN}\right) = A\left(\Delta K\right)^n \tag{6}$$

where a is the crack length; N is the number of loading cycles; A, n are material parameters; ΔK is the change in SIF.

To accommodate viscoelastic nature of HMA materials, researchers implemented energy dependent crack propagation models (21-23). Change in Strain Energy and Fracture Energy over number of cycles are defined as Strain Energy Release $\left(\Delta U\right)$ and Fracture Energy Release $\left(\Delta G\right)$ respectively.

For RCIP-VI test data, a modified Paris and Erdogan Law was proposed by replacing SIF $\left(\Delta K\right)$ by ΔG and ΔU as follows:

$$\left(\frac{da}{dN}\right) = A\left(\Delta U\right)^n \tag{7}$$

$$\left(\frac{da}{dN}\right) = A\left(\Delta G\right)^n \tag{8}$$

Note that ΔU and ΔG are both function of load, crack geometry, material properties, and overlay geometry.

Table 4 tabulates the number of loading cycle and crack length from distress survey. Material parameters *A* and *n* were then determined through regression analysis on the average crack propagation rate values of north and south section. As shown in Figure30 and Figure31, positive values of *A* and *n* indicated that crack propagation rate increased with increase in both Strain Energy Release and Fracture Energy Release. Values of the parameters, such as CPR (da/dN), ΔU and ΔG, related to Figure30 and 31 are shown in table 3 and 4 of Appendix B. It was observed that *A* and *n* followed the similar trend as reported in literature (20). Note that the reported values were derived from Paris and Erdogan law based on SIF, whereas in this report Paris and Erdogan law was modified based on ΔU and ΔG.

Table 4. Summary of Crack Length and Cycle Number

North				South	
Outer		Inner		Inner	
Cycle Number	Crack Length, in.	Cycle Number	Crack Length, in.	Cycle Number	Crack Length, in.
320	1.125	320	1.125	480	1.125
480	2.250	480	2.000	565	2.25
565	2.500	1169	4.250	1160	3.500
800	3.500	2550	5.000	1284	3.625
1160	5.000			1660	4.250
				2100	5.000

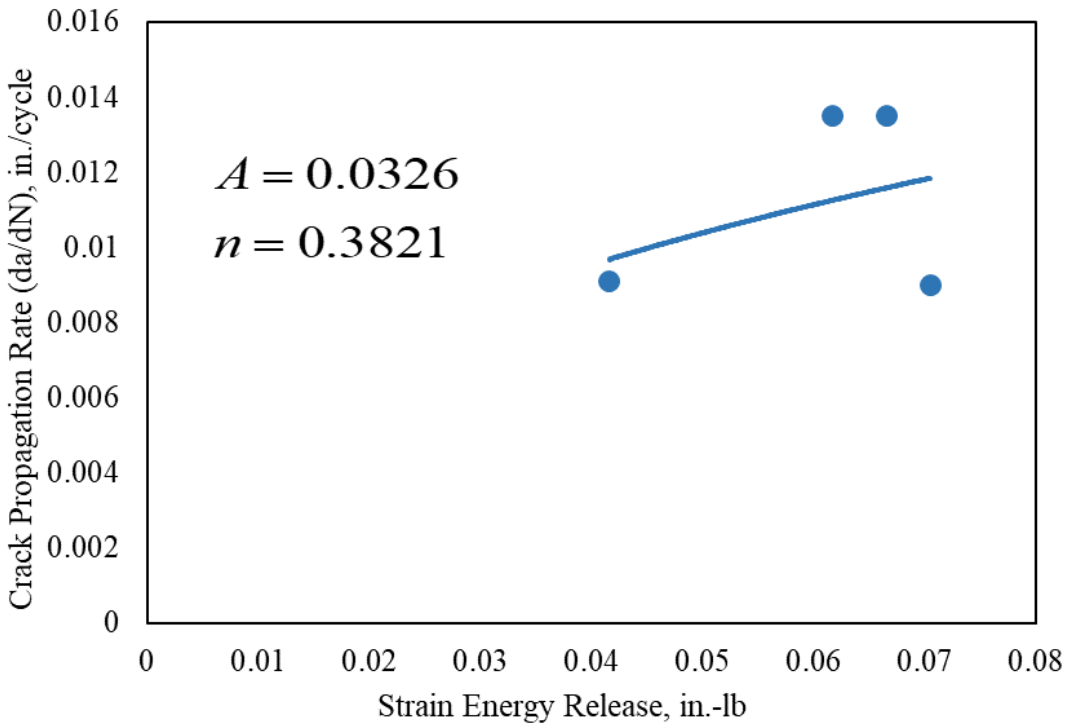

Figure30. Crack Propagation Rate vs. Strain Energy Release (Detailed calculations are summarized in table 3 of Appendix B)

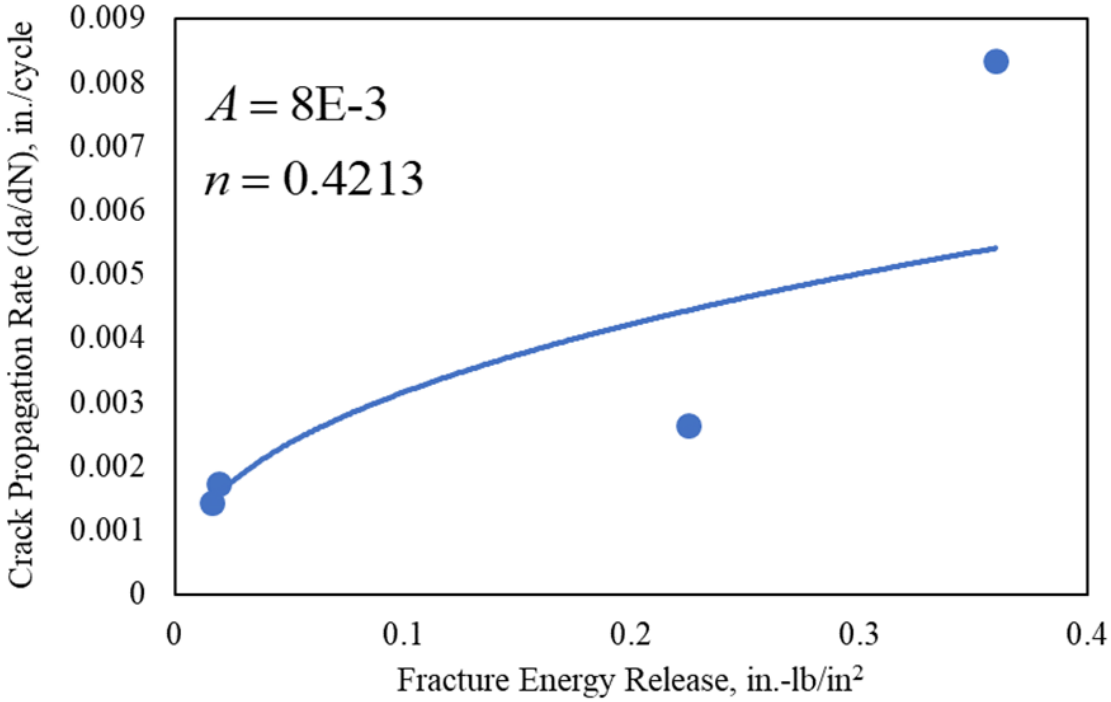

Figure31. Crack Propagation Rate vs. Fracture Energy Release (Detailed calculations are summarized in table 4 of Appendix B)

8. EFFECT OF EXTREME COOLING CYCLE

8.1 STRAIN RESPONSE

Based on the peak strain from the loading cycle preceding and succeeding the extreme cooling cycles, the (%) Increase in Strain Response was calculated as follows:

$$(\%)\ \text{Increase in Strain Response} = \frac{\varepsilon_{\text{preceding}} - \varepsilon_{\text{succeeding}}}{\varepsilon_{\text{preceding}}} \times 100 \qquad (9)$$

where $\varepsilon_{succeeding}$ and $\varepsilon_{preceding}$ are peak strain responses at the cycle number preceding and succeeding the extreme cooling cycles, respectively. Most of the strain gages had failed before the start of 2nd set of extreme cooling cycles, the analysis was therefore limited to the 1st set of extreme cooling cycles. In general, a noticeable effect of extreme cooling cycles was found in the strain responses. One of such examples is provided in Figure32. Few more of such examples are provided in Appendix B (Figure1 and Figure2). Figure33 compares the average percentage (%) increase in strain responses at bottom, mid-depth, and surface of the overlay. The highest (%) increase was at the surface (17%) followed by mid-depth (11%) and bottom (7%). The (%) increase in strain response for all the gages is provided in table 5 of Appendix B. Given the time and temperature dependency of AC materials (Figure14), the negative temperature gradient could have rendered the upper portion of overlay more susceptible to the higher loading rate.

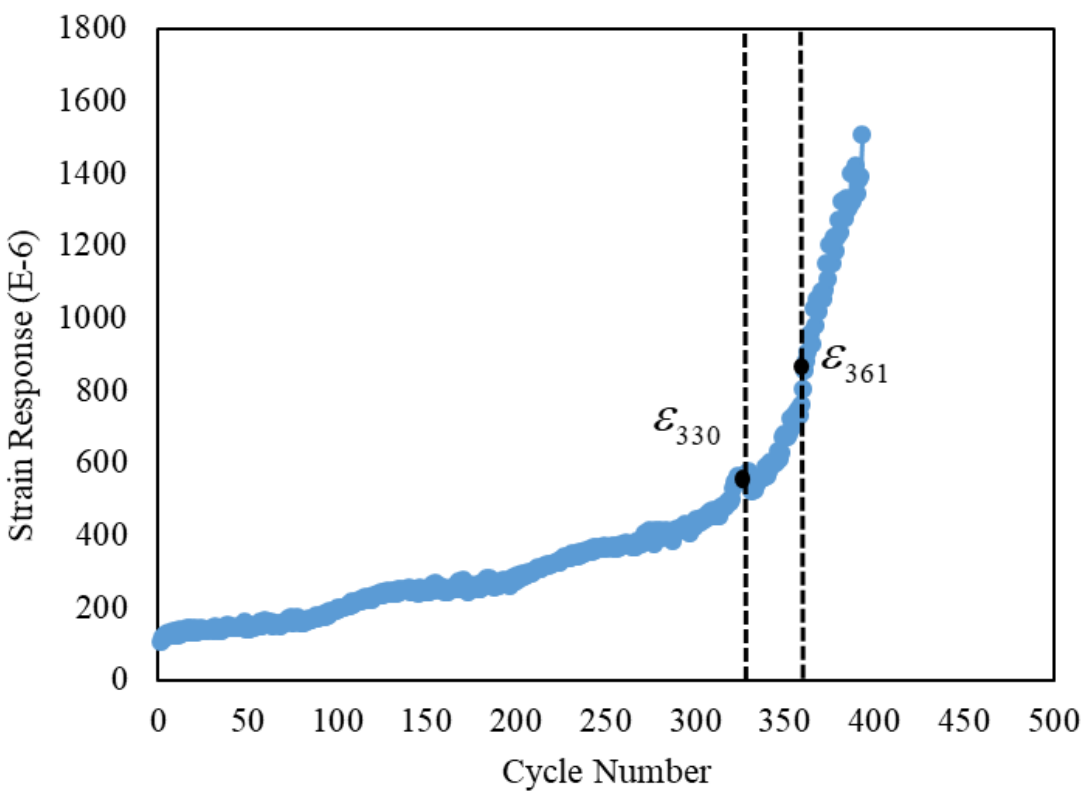

Figure32. Peak Strain Response in SG3-N-5

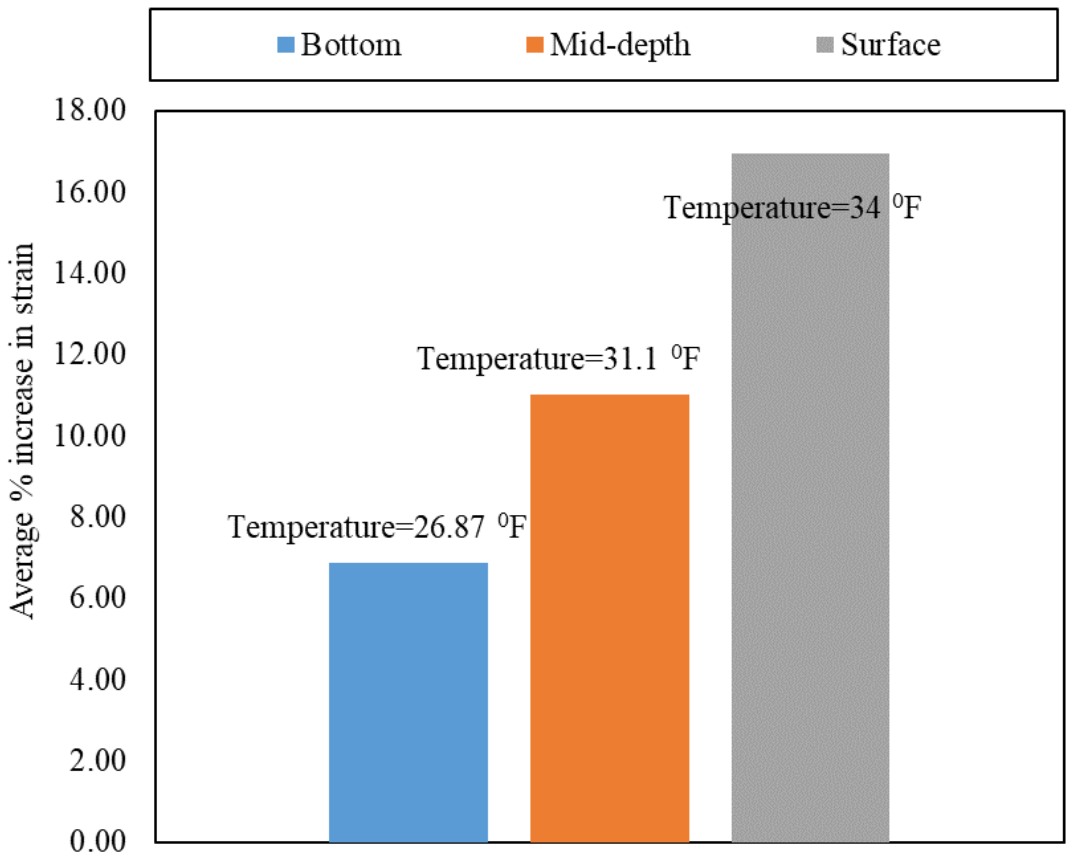

Figure33. Average Percent Increase in Strain Response at Different Depths (Detailed calculations are summarized in table 5 of Appendix B)

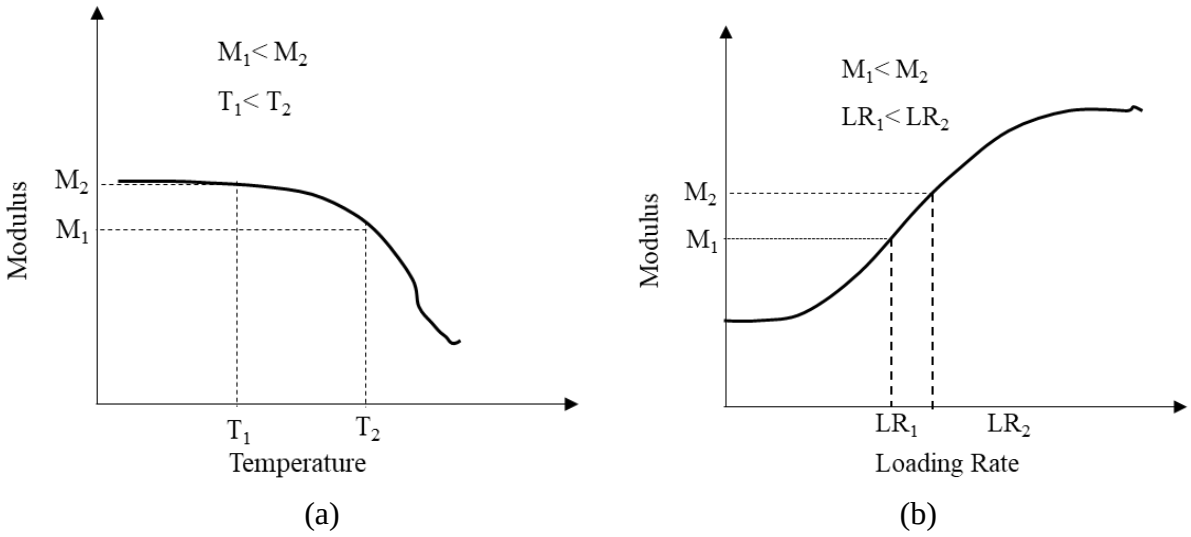

Figure34. Viscoelastic Behavior of AC Materials under the effect of (a) Temperature and (b) Loading rate

8.2 STRAIN ENERGY

Figure35 illustrates two quantities defined as follows:

$$(\%)\ \text{increase in } U_{\text{Damaged}} = \frac{U_{\text{Damaged,extreme}} - U_{\text{Damaged,preceding}}}{U_{\text{Damaged,preceding}}} \times 100 \tag{10}$$

$$(\%)\ \text{decrease in } U_{\text{Damaged}} = \frac{U_{\text{Damaged,extreme}} - U_{\text{Damaged,succeeding}}}{U_{\text{Damaged,extreme}}} \times 100 \tag{11}$$

where $U_{\text{Damaged, extreme}}$ is the average of U_{Damaged} during 30 extreme cooling cycles, $U_{\text{Damaged, preceding}}$ is the average of U_{Damaged} during the preceding 30 loading cycles and $U_{\text{Damaged, succeeding}}$ is the average of U_{Damaged} during the succeeding 30 loading cycles. As mentioned earlier, most of the strain gages had failed before the start of 2nd set of extreme cooling cycles, limiting the analysis to the 1st set of extreme cooling cycles. Figure35 shows the portion of U_{Damaged} from Figure27 that captures the 1st set of extreme cooling cycle i.e., between 300 and 390 loading cycles. Figure35 reveals a higher energy release due to extreme cooling cycles and resulted in more damage because (%) decrease in $U_{Damaged}$ was higher compared to (%) increase.

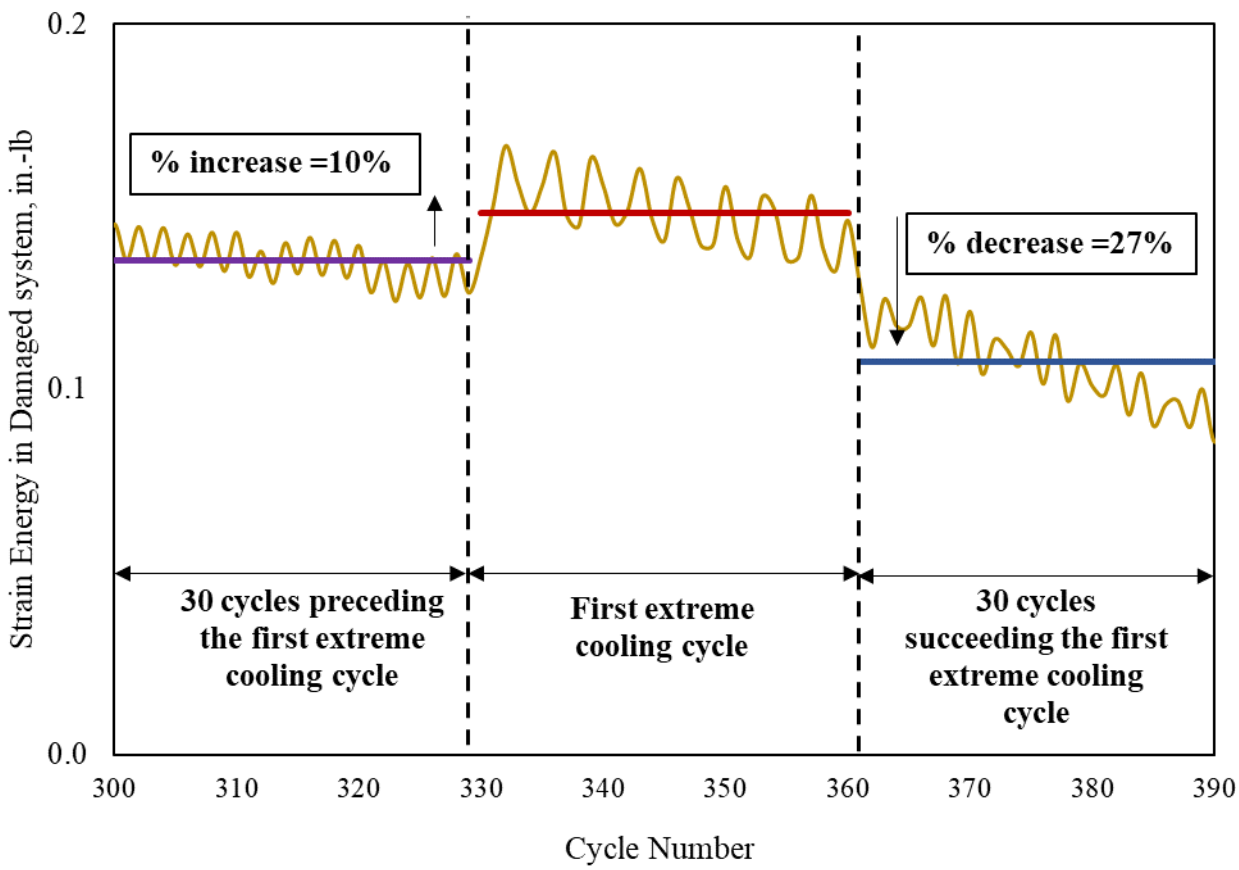

Figure35. Strain Energy Preceding, During, and Succeeding the 1st set of Extreme Cooling Cycles

8.3 FRACTURE ENERGY

For Fracture Energy, Figure36 illustrates two quantities defined as follows:

$$(\%)\ \text{increase in } G = \frac{G_{\text{extreme}} - G_{\text{preceding}}}{G_{\text{preceding}}} \times 100 \tag{12}$$

$$(\%)\ \text{decrease in } G = \frac{G_{\text{extreme}} - G_{\text{succeeding}}}{G_{extreme}} \times 100 \tag{13}$$

where $G_{extreme}$ is the average of G during 30 extreme cooling cycles, $G_{preceding}$ is the average of G during the preceding 30 loading cycles and $G_{succeeding}$ is the average of G during the succeeding 30 loading cycles.

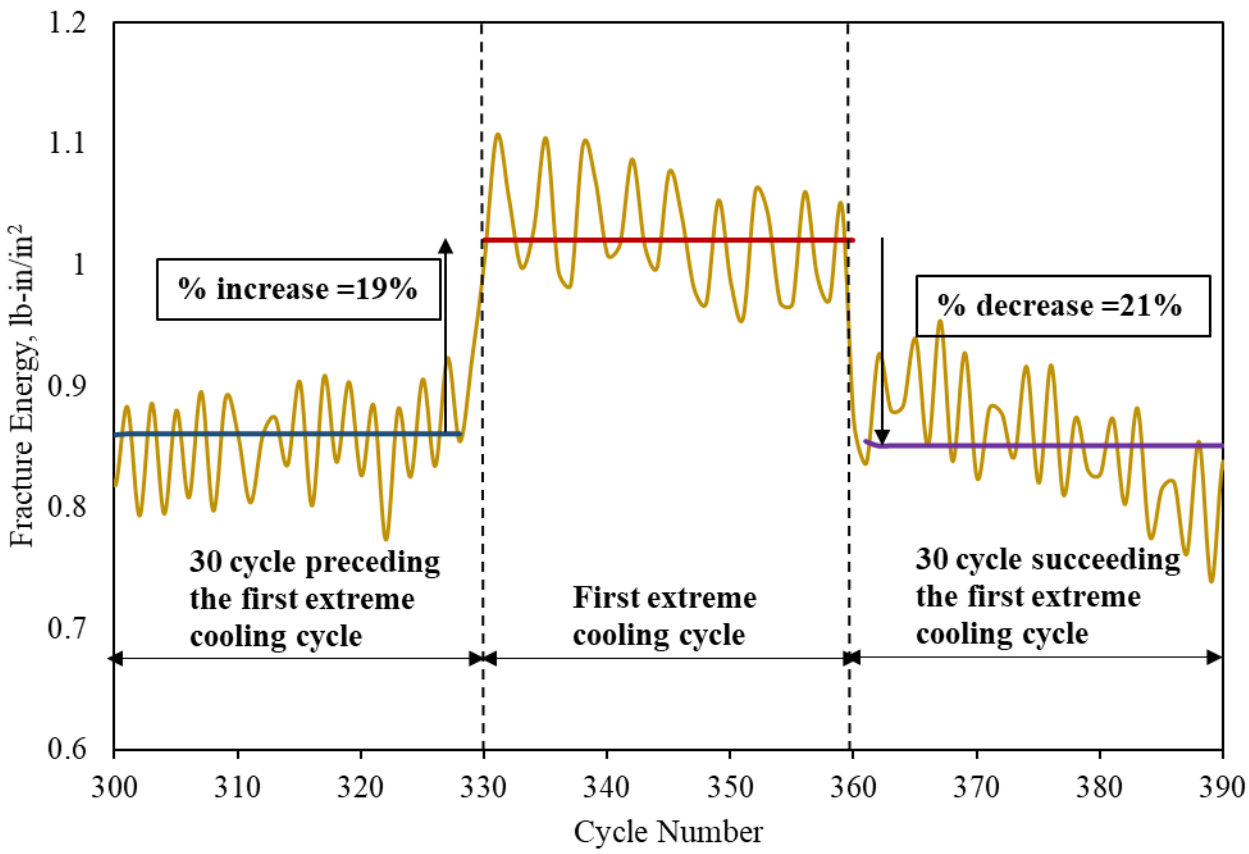

Figure36. Fracture Energy Preceding, During, and Succeeding Extreme Cooling Cycles

As mentioned earlier, due to a power outage, data was not available for the 3rd set of extreme cooling cycles. As shown in Figure37, both the (%) decrease and (%) increase reduced at higher loading cycles because of increasing fracture energy release from the crack evolution. The reduction in load carrying capability of AC overlay also resulted in that the (%) decrease after extreme cooling cycles was always higher than the (%) increase. This observation is consistent with Figure35.

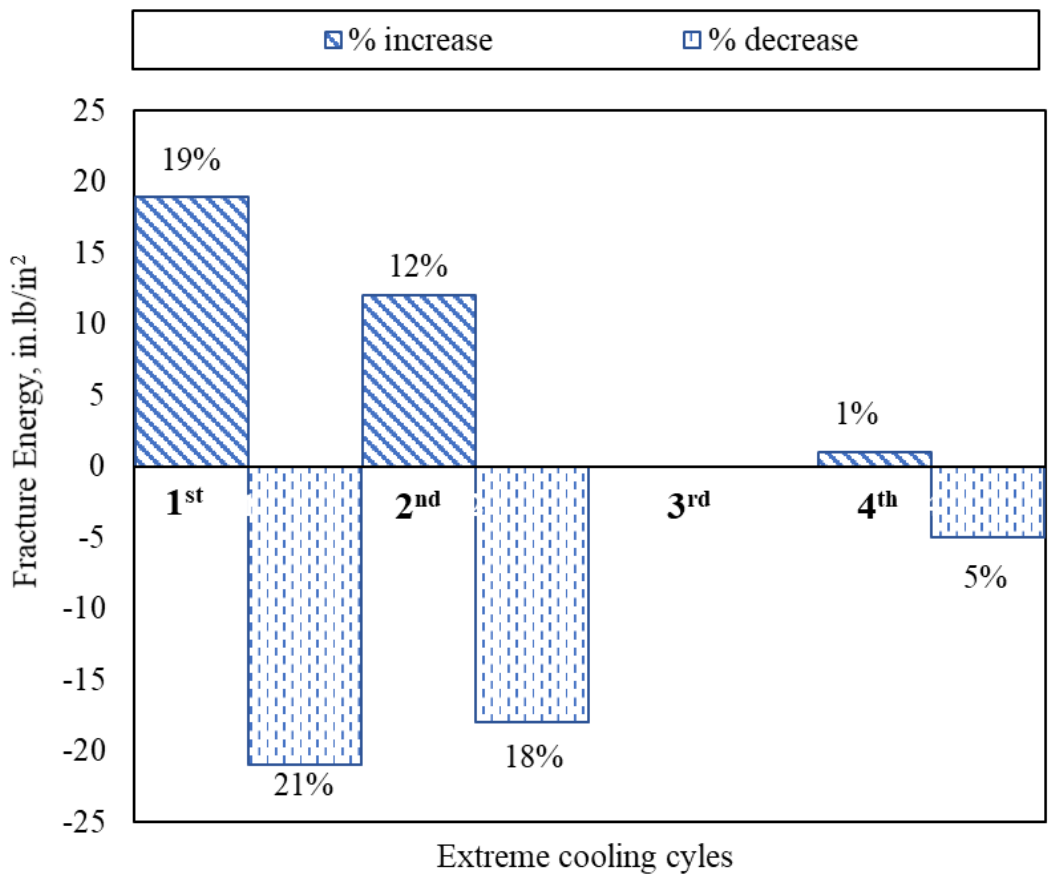

Figure37. Percentage Change in Fracture Energy

9. IMPLEMENTATION OF RCIP-VI TEST DATA

In support of the modeling effort of crack propagation, the following 3 steps are proposed for future implementation of RCIP-VI full-scale test data.

9.1 STEP 1: CRACK INITIATION

The Finite Element Model (FEM) was previously developed to facilitate Reflective Cracking Outdoor Phase-1 (RCOP-I) Test Plan (26). Indoor full-scale reflective cracking tests were limited to a temperature loading study, whereas outdoor experiment considers both aircraft and temperature loading. The overlay experiences horizontal stress/strain due to the temperature variation and it leads to Mode I fractures. Under the wheel loading, vertical shear stress/strain is observed in addition to the horizontal stress/strain at the bottom of the HMA overlay leading to Mode II fractures. Under the temperature and traffic loading, horizontal stress/strain are more enhanced compared to the traffic loading, in addition to vertical shear stress/strain, leading to Mode II fractures (3). In conventional practices, characterization of vertical shear stress (and/or strain) of HMA is barely observed and supporting evidence is not readily available for Mode II fractures. Consequently, only Mode I fractures were considered. Therefore, to estimate the number of loading cycles to crack initiation, the indoor full-scale test data used a strain-based criterion of

1800 microstrain instead of advanced fatigue models (such as Viscoelastic Continuum Damage model (24)). Full-scale test data analysis of RCIP-VI provided the possibility of energy based criterions: Critical Strain Energy and Critical Fracture Energy for modeling crack initiation (see Table 5).

9.2 STEP 2: CRACK PROPAGATION

A modified Paris and Erdogan Law (e.g., based on ΔU and ΔG) was employed to quantify the crack propagation rate of RCIP-VI test overlay. Both sets of the material parameters (i.e., A and n) are recommended to be considered in the modeling of the crack propagation (see Table 5).

Table 5. Summary of Step 1 and 2 Implementation

Crack Initiation		Crack Propagation
Critical Strain Energy	0.23 in.lb	Modified Paris and Erdogan law based on ΔU A=0.0326 n=0.3821
Critical Fracture Energy	0.9 in.lb/in^2	Modified Paris and Erdogan Law based on ΔG A=8E-3 n=0.4213

9.3 STEP 3: FINITE ELEMENT MODEL VALIDATION

Figure38 plots the crack length vs. cycle number of north and south sections of RCIP-VI test overlay. A difference in cycle number between the two test sections was observed, which was inherited from the loading difference as observed in Figure21; however, crack propagation followed almost identical trend. The crack length remained at a slow increase rate until it reached the upper portion of the overlay. As the propagation of reflection cracks became aggressive (steep slope), much lesser number of loading cycles were required. Similar observations were reported from the previous NAPTF studies (Figure24 of (5), Figure23 of (4), and Figure12 of (25)). The previously developed FEM for RCOP-I should be validated by comparing simulated crack propagation against the RCIP-VI test observations.

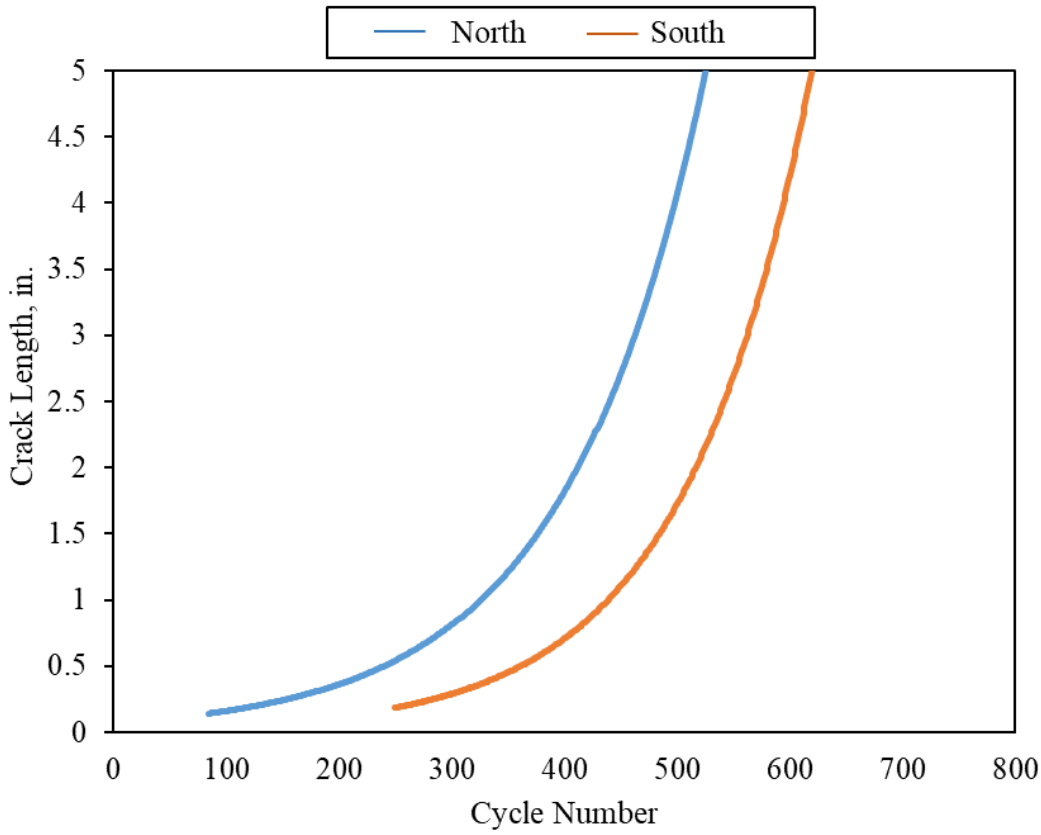

Figure38. Crack Length vs. Cycle Number

10. CONCLUSIONS

The RCIP-VI test overlay consisted of two sections built with identical AC materials, using the standard FAA P-401 HMA (PG 64-22), and of equal thicknesses of 5 in. To evaluate the effect of extreme cooling cycle on the crack initiation and propagation, two distinct displacement rates were simulated by the TESS. General test observations such as crack sequencing, failure strain, and crack evolution agreed well to the previous experiments. Analysis of the results of RCIP-VI test data included the following:

1. Effect of extreme cooling cycles was prominent on the strain gage responses.
2. Effect of extreme cooling cycle was identified and quantified through Strain Energy and Fracture Energy analysis. Both demonstrated the energy release during the crack propagation and associated overlay weakening.
3. To characterize the crack propagation, the Paris and Erdogan Law was first modified using Strain Energy Release and Fracture Energy Release. Then material properties, *A* and *n*, were derived.

Lastly, future implementation of RCIP-VI full-scale test data to the modeling effort of crack initiation and propagation was proposed.

11. REFERENCES

1. Bennert, T., (2009) " A rational approach to the prediction of reflective cracking in Bituminous overlays for concrete pavements," *Rutgers University, Graduate School, New Brunswick.*
2. Bozkurt, D. and Buttlar, W.G., "Three-dimensional finite element modeling to evaluate benefits of interlayer stress absorbing composite for reflective crack mitigation," in *Proc., Federal Aviation Administration Airport Technology Transfer Conference*. 2002.
3. Lytton, R.L., et al. (2010) "Models for predicting reflection cracking of hot-mix asphalt overlays. 2010," *Report no. 669*
4. Yin, H. (2017) Reflective Cracking Phase II Comprehensive Report.
5. Yin, H. (2017) Reflective Cracking Phase V Comprehensive Report.
6. Song, S.H., Paulino, G.H., and Buttlar, W.G., (2006) "Simulation of crack propagation in asphalt concrete using an intrinsic cohesive zone model," *Journal of Engineering Mechanics, 132(11): p. 1215-1223.*
7. Yin, H. (2017) Reflective Cracking Phase IV Comprehensive Report.
8. Yin, H. and Barbagallo, D. (2013) "Development of full-scale reflective cracking test at the FAA National Airport Pavement Test Facility," *Transportation Research Record, 2368(1): p. 81-91.*
9. Griffith, A.A. (1921) VI. "The phenomena of rupture and flow in solids," *Philosophical transactions of the royal society of london. Series A, containing papers of a mathematical or physical character, 221(582-593): p. 163-198.*
10. Birgisson, B., et al., (2007) " Numerical implementation of a strain energy-based fracture model for HMA materials," *Road materials and pavement design*, 2007. **8**(1): p. 7-45.
11. Tang, S., (2014) " Evaluate the fracture and fatigue resistances of hot mix asphalt containing high percentage reclaimed asphalt pavement (RAP) materials at low and intermediate temperatures,"*Iowa State University.*
12. Garcia, V., et al. (2017) "Improved overlay tester for fatigue cracking resistance of asphalt mixtures," *Center for Transportation Infrastructure Systems. Report No*. 2017, TxDOT 0-6815-1.
13. TxDOT, *Test Procedure for Overlay Test.* 2019. TxDOT Designation: Tex-248-F.
14. Paris, P. and Erdogan, F. (1963) "A critical analysis of crack propagation laws," *Journal of basic engineering*, 85(4): p. 528-533.
15. Gray, B. and Martin, G. (1933) "Resurfacing with bituminous types of surfaces," *Highway Research Board Proceedings*. 1933.
16. Jayawickrama, P.W., (1985) "Methodology for predicting asphalt concrete overlay life against reflection cracking. (1985)." *Texas A&M University.*
17. Lytton, R.L., et al. (1993) Development and validation of performance prediction models and specifications for asphalt binders and paving mixes. Vol. 357: *Strategic Highway Research Program Washington, DC*.
18. Monismith, C. and Coetzee, N. (1980) "Reflection cracking: analyses, laboratory studies, and design considerations," *Association of Asphalt Paving Technologists Proceedings*.
19. Nunn, M. (2009) "An investigation of reflection cracking in composite pavements in the United Kingdom." *Reflective Cracking In Pavements*.
20. Zhou, F., et al. (2009) "Mechanistic-empirical asphalt overlay thickness design and analysis system," *Texas Transportation Institute.*

21. Schapery, R. (1973) “A theory of crack growth in viscoelastic media,” *Texas A And M Univ College Station Mechanics And Materials Research Center*.
22. Schapery, R. (1978) “A method for predicting crack growth in nonhomogeneous viscoelastic media,” *International Journal of Fracture, 14(3): p. 293-309*.
23. Schapery, R.A. (1984) “Correspondence principles and a generalizedJ integral for large deformation and fracture analysis of viscoelastic media,” *International Journal of Fracture, 1984. 25(3): p. 195-223.*
24. Park, S.W., Kim, Y.R. and Schapery, R.A., 1996. A viscoelastic continuum damage model and its application to uniaxial behavior of asphalt concrete. *Mechanics of Materials*, *24*(4), pp.241-255.
25. Yin, H. (2017) Reflective Cracking Phase III Comprehensive Report.

APPENDIX A. DISTRESS SURVEY WRITTEN LOG

Date	Total Cycles		Daily Cycles	Distress						
				Description	No.	Location				
						X Axis (in.)		Y Axis (in.)		Location
	North	South				Initial	End	Initial	End	
6/10/2019	320	320	120	Bottom-up crack	1	2.875	2.875	0	1.125	Outer vertical edge, North
6/10/2019	320	320	120	Transverse surface crack	2	16	47.5	2.5	4.625	North section
6/10/2019	320	320	120	Bottom-up crack	3	2.875	3.125	0	1.125	Inner vertical edge, North
6/11/2019	480	480	120	Bottom-up crack	4	2.875	3.25	1.125	2.25	Outer vertical edge, North
6/11/2019	480	480	120	Transverse surface crack	5	11.5	16	3	3.62	North section
6/11/2019	480	480	120	Bottom-up crack	6	2.25	2.875	1.125	2	Inner vertical edge, North
6/11/2019	480	480	120	Bottom-up crack	7	2.75	2.875	0	1	Inner vertical edge, South
6/12/2019	565	565	120	Bottom-up crack	8	3	3	2.25	2.5	Outer vertical edge, North
6/12/2019	565	565	120	Transverse surface crack	9	47.5	48.5	3	3.75	North section
6/12/2019	565	565	120	Bottom-up crack	10	2.25	2.5	2	2.25	Inner vertical edge, North
6/12/2019	565	565	120	Bottom-up crack	11	2.75	3.125	1	2.25	Inner vertical edge, South
6/12/2019	565	565	120	Transverse surface crack	12	14	34.75	2	4	South section
6/12/2019	595	595	120	Transverse surface crack	13	4.5	11.5	2.625	4	North section
6/12/2019	595	595	120	Transverse surface crack	14	34.75	37.5	2.75	3.25	South section
6/13/2019	680	680	120	Transverse surface crack	15	3.625	4.5	3	3.375	North section
6/13/2019	680	680	120	Transverse surface crack	16	48.5	52.375	3	4	North section
6/13/2019	680	680	120	Transverse surface crack	17	11	14	2.25	3.75	South section
6/13/2019	680	680	120	Transverse surface crack	18	37.5	49	2.625	3.875	South section
6/13/2019	725	725	120	Transverse surface crack	19	52.375	55	3	3.5	North section
6/14/2019	800	800	120	Bottom-up crack	20	3.5	3.75	3	3.5	Outer vertical edge, North
6/14/2019	800	800	120	Transverse surface crack	21	3	3.625	3	3.5	North section
6/14/2019	800	800	120	Transverse surface crack	22	5	11	2.75	3.5	South section
6/14/2019	800	800	120	Transverse surface crack	23	49.5	53	2.875	3.125	South section
6/17/2019	1160	1160	120	Bottom-up crack	24	2.5	3.625	2.5	4.25	Outer vertical edge, North
6/17/2019	1160	1160	120	Bottom-up crack	25	3.375	4	3.5	4	Outer vertical edge, North
6/17/2019	1160	1160	120	Bottom-up crack	26	3.5	3.75	4	5	Outer vertical edge, North
6/17/2019	1160	1160	120	Transverse surface crack	27	0	3	2.5	2.875	North section
6/17/2019	1160	1160	120	Bottom-up crack	28	2.625	3	1.75	2.75	Inner vertical edge, North
6/17/2019	1160	1160	120	Bottom-up crack	29	3	3.375	3.375	4.25	Inner vertical edge, North

Date	Total Cycles		Daily Cycles	Distress						
				Description	No.	Location				
						X Axis (in.)		Y Axis (in.)		Location
	North	South				Initial	End	Initial	End	
6/17/2019	1160	1160	120	Bottom-up crack	30	3.75	1.75	4.25	2.75	Inner vertical edge, North
6/17/2019	1160	1160	120	Bottom-up crack	31	4.25	2.25	5.625	2.75	Inner vertical edge, North
6/17/2019	1160	1160	120	Bottom-up crack	32	5	6	1	1.5	Inner vertical edge, North
6/17/2019	1160	1160	120	Bottom-up crack	33	3	2.375	3.25	3.5	Inner vertical edge, South
6/17/2019	1160	1160	120	Bottom-up crack	34	2.875	0	3.25	3	Outer vertical edge, South
6/18/2019	1284	1284	120	Bottom-up crack	35	0	2.75	0.5	1	Outer vertical edge, North
6/18/2019	1284	1284	120	Transverse surface crack	36	55	58	2.75	3	North section
6/18/2019	1284	1284	120	Bottom-up crack	37	2.5	3.125	3.375	3.625	Inner vertical edge, South
6/18/2019	1284	1284	120	Transverse surface crack	38	3	5	2.375	3.375	South section
6/18/2019	1284	1284	120	Transverse surface crack	39	52.5	54.25	2.875	3	South section
6/19/2019	1388	1388	120	Bottom-up crack	40	4	4.625	2.25	2.5	Inner vertical edge, south
6/20/2019	1515	1515	120	Transverse surface crack	41	1.5	2.5	2.5	3	South section
6/20/2019	1515	1515	120	Transverse surface crack	42	55	56.5	1.25	1.5	South section
6/21/2019	1660	1660	120	Bottom-up crack	43	2	2.5	3.5	4.25	Inner vertical edge, South
6/21/2019	1660	1660	120	Transverse surface crack	44	0.75	1.5	3.5	3.5	South section
6/21/2019	1660	1660	120	Transverse surface crack	45	56.5	57	1.375	1.375	South section
6/24/2019	1724	1724	210	Bottom-up crack	46	5.125	6			Inner vertical edge, South
6/27/2019	2100	2100	120	Bottom-up crack	47	2	2.375	4.25	5	Inner vertical edge, South
6/27/2019	2100	2100	120	Transverse surface crack	48	0	0.5	3.75	3.75	South section
7/1/2019	2550	2550	120	Bottom-up crack	49	3.25	3.5	4	4.75	Inner vertical edge, North
7/1/2019	2550	2550	120	Transverse surface crack	50	58	59.5	3	3	North section
7/3/2019	2820	2820	120	Bottom-up crack	51	3.5	3.5	4.75	5.25	Inner vertical edge, North
7/3/2019	2820	2820	120	Transverse surface crack	52	58.5	59.5	3	3	North section
7/8/2019	3200	3200	120	Transverse surface crack	53	59.5	60	3	3.5	North section
7/16/2019	4015	4015	120	Transverse surface crack	54					

APPENDIX B. DETAILS OF ANALYSIS

Table 1. Crack Propagation Rate

	North		South	
	Horizontal	Vertical	Horizontal	Vertical
Crack Length (in.)	24	5	24	5
Average Number of Cycles	218	385	320	333
Crack Propagation Rate (CPR) (in./cycle)	0.11	0.013	0.075	0.015

Table 2: Demonstration of steps for calculating $U_{Undamaged}$ and $U_{Damaged}$

(a): Step 1

Step 1:	Cycle Number	Bottom SG: SG6-N-0 (microstrain)	Mid-Depth SG: SG6-N-2.5 (microstrain)	Top SG: SG6-N-5 (microstrain)	Average strain (microstrain)
	1	200	417	1314	644
	361	330	752	1378	820

(b): Step 2

Step 2:	Cycle Number	Peak Load (Load cell readings), lbs	Area, in.^{2}	Stress, psi
	1	66588	300	222
	361	37645	300	126

(c): Step 3

Step 3:	Cycle Number	Stress, psi	Average Strain (microstrain)	Depth (d), in.	Effective depth (d'), in.	$U_{Undamaged}$ in.-lb	$U_{Damaged}$ in.-lb
	1	222	644	5	5	0.357	0.357
	361	126	820	5	2.5	0.257	0.129

Table 3: Calculation details for Figure30.

Crack length (a), in.	Number of cycles	da, in.	dN	U, in.-lb	ΔU , in.-lb
0.5	56	1	111	0.2407	0.0705
1.5	167	1	110	0.1702	0.0416
2.5	277	1	74	0.1286	0.0665
3.5	351	1.5	111	0.0621	0.0617
5	462			0.0004	

Table 4: Calculation details for Figure31.

Crack length (a), in.	Number of cycles	da, in.	dN	G, in.-lb/in^2	ΔG , in.-lb/in^2
1.125	373	1.125	135	0.84	0.36
2.25	508	1.25	472	0.48	0.225
3.5	980	0.75	435	0.255	0.019
4.25	1415	0.75	522	0.236	0.016
5	1937			0.22	

Table 5(a): (%) increase in strain during the 1st set of extreme cooling cycle at the surface of the overlay.

SGs at Top			
Sensor ID	$\varepsilon_{preceeding}$	$\varepsilon_{succeeding}$	(%) increase
SG1-N-5.0	247	219	13
SG2-N-5.0	312	271	15
SG3-N-5.0	857	567	51
SG4-N-5.0	788	558	41
SG5-N-5.0	403	371	9
SG6-N-5.0	330	311	6
SG1-S-5.0	250	213	17
SG2-S-5.0	229	201	14
SG3-S-5.0	524	428	22
SG4-S-5.0	332	301	10
SG5-S-5.0	255	251	2
SG6-S-5.0	251	246	2

Table 5(b): (%) increase in strain during the 1st set of extreme cooling cycle at mid-depth of the overlay.

SGs at Mid-depth			
Sensor ID	$\varepsilon_{preceeding}$	$\varepsilon_{succeeding}$	(%) increase
SG1-N-2.5	570	496	15
SG6-N-2.5	752	678	11
EG2-N-2.5	785	687	14
EG3-N-2.5	1297	1121	16
EG4-N-2.5	1428	1253	14
EG5-N-2.5	874	804	9
SG1-S-2.5	496	419	18
SG6-S-2.5	411	402	2
EG2-S-2.5	765	672	14
EG3-S-2.5	1089	1008	8
EG4-S-2.5	1130	1062	6
EG5-S-2.5	622	592	5

Table 5(c): (%) increase in strain during the 1st set of extreme cooling cycle at the bottom of the overlay.

SGs at Mid-depth			
Sensor ID	$\varepsilon_{preceeding}$	$\varepsilon_{succeeding}$	(%) increase
EG2-N-0	1594	1462	9
EG3-N-0	1825	1733	5
EG4-N-0	1913	1818	5
EG5-N-0	1727	1633	6
SG1-S-0.0	1116	975	14
EG2-S-0	1454	1333	9
EG3-S-0	1637	1578	4
EG4-S-0	1798	1739	3
EG5-S-0	1451	1397	6

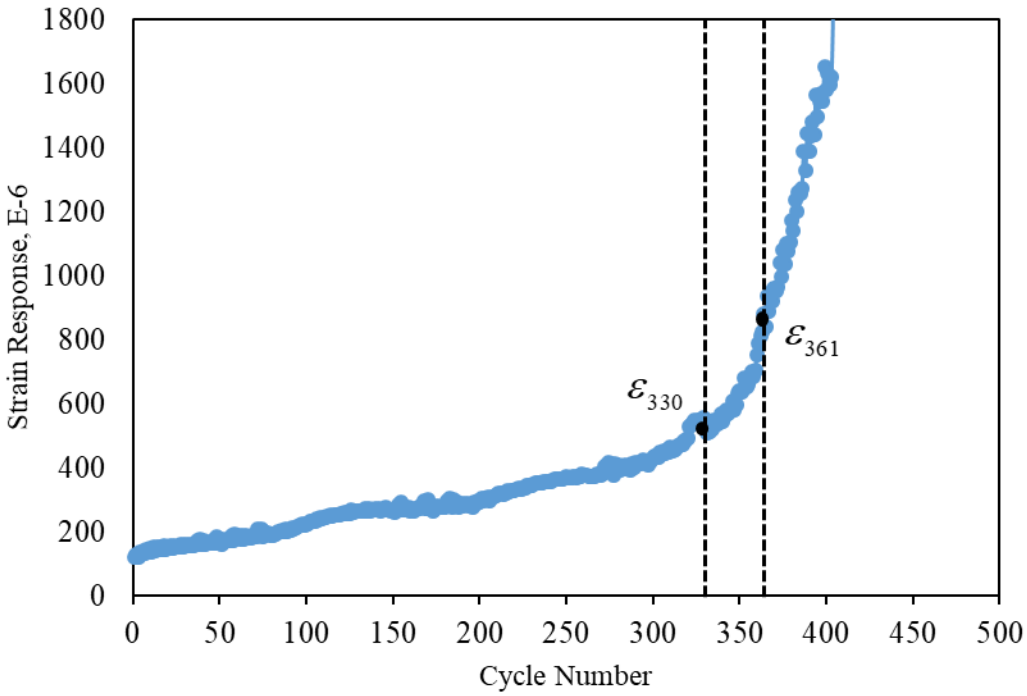

Figure1. Peak Strain Response in SG4-N-5

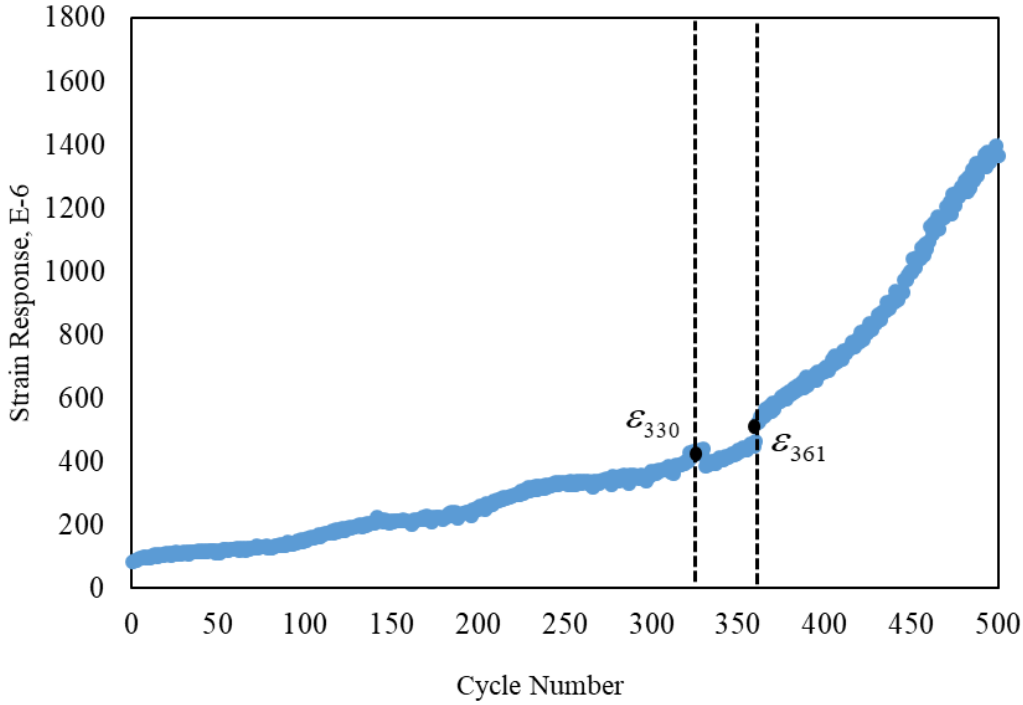

Figure2. Peak Strain Response in SG3-S-5